Vehicle-to-Vehicle Communications in Mixed Passenger-Freight Convoys

Final Report

METRANS Project 14-11

September 2016

Andreas Molisch (Principal Investigator)
Olivier Renaudin (Co-Principal Investigator)
Rui Wang (Ph.D. Student)
He Zeng (Ph.D. Student)

Ming Hsieh Department of Electrical Engineering
Viterbi School of Engineering - University of Southern California
Los Angeles, CA 90089-2565

Disclaimer

The contents of this report reflect the views of the authors who are responsible for the facts and the accuracy of the data presented herein. The contents do not necessarily reflect the official views or policies of the STATE OF CALIFORNIA or the FEDERAL HIGHWAY ADMINISTRATION. This report does not constitute a standard, specification, or regulation.

Abstract

Vehicle convoys (platoons) hold a promise for significant efficiency improvements of freight and passenger transportation through better system integration. Through the use of advanced driver assistance, vehicles in a convoy can keep shorter distances from each other, thus decreasing energy consumption and traffic jams. However, reliable and low-latency communications are a vital prerequisite for such systems.

The standard for Vehicle-to-Vehicle (V2V) wireless communications is IEEE 802.11p, and its performance for communication between passenger cars has been widely explored. However, there are hardly any results about the performance of such systems when both trucks and passenger cars are present. In order to remedy this situation, we first perform in the framework of this project extensive measurement campaigns of the propagation channel between cars and trucks, and between cars whose connection is blocked by trucks. These scenarios are clearly of great importance for mixed-traffic convoys, yet have not yet been explored or measured in the open literature. For that purpose, we constructed antenna arrays in order to characterize the double directional characteristics of the underlying propagation channel, as well as a wideband and directional channel sounder with high precision synchronization based on software defined radio platforms. The measured data are then used as the inputs of a IEEE 802.11p communication system simulator, which tells us not only the probability of successful communication between vehicles but also helps to analyze robust methods such as multi-hop to resolve the situations where direct communications are not successful. Its outputs constitute an important input for the design of convoy policies, enhanced automated driver assistance, and even self-driving cars.

Contents

List of Figures

List of Tables

List of Acronyms

AC	Access Category
ACK	Acknowledgment
AIFS	Arbitration Inter Frame Space
AOA	Azimuth-of-Arrival
AOD	Azimuth-of-Departure
AP	Access Point
APS	Angular Power Spectrum
AWGN	Additive White Gaussian Noise
BER	Bit Error Rate
BSS	Basic Service Set
BSSID	Basic Service Set Identification
CDF	Cumulative Density Function
CRC	Cyclic Redundancy Check
CSI	Channel State Information
CSMA/CA	Carrier Sense Multiple Access with Collision Avoidance
CTS	Clear To Send
CW	Contention Window
DAC	Digital-to-Analog Converter
DCF	Distributed Contribution Function
DIFS	Distributed Inter Frame Space
DMC	Diffuse Multipath Component
DS	Delay Spread
EDCA	Enhanced Distributed Channel Access
EDCAF	Enhanced Distributed Channel Access Function

FCS	Frame Check Sequence
FER	Frame Error Rate
FFT	Fast Fourier Transform
GSCM	Geometry-based Stochastic Channel Model
GPS	Global Positioning System
ICI	Inter Carrier Interference
i.i.d.	independent identically distributed
IFFT	Inverse Fast Fourier Transform
IFS	Inter Frame Space
IR	Impulse Response
ISI	Inter-Symbol Interference
ITS	Intelligent Transportation Systems
LLR	Log-Likelihood Ratio
LO	Local Oscillator
LOS	Line-Of-Sight
LS	Least Square
LTE	Long Term Evolution
MAC	Medium Access Control
MD	mobile scatterer
MLE	Maximum Likelihood Estimator
MIMO	Multiple-Input Multiple-Output
MPC	Multipath Component
MSDU	MAC Service Data Unit
NAV	Network Allocation Vector
NLOS	Non-Line-of-Sight
OFDM	Orthogonal Frequency Division Multiplexing
PDF	Probability Density Function
PDP	Power-Delay Profile
PHY	Physical Layer
PLCP	Physical Layer Convergence Protocol

PMD	Physical Medium Dependent
PPDU	PLCP Protocol Data Unit
PPS	Pulse Per Second
PSDU	PLCP Service Data Unit
QoS	Quality of Service
RF	Radio-Frequency
RTS	Ready To Send
Rx	Receiver
RMS	Root Mean Square
SAGE	Space-Alternating Generalized Expectation-Maximization
SD	static scatterer
SP	specular path
S/P	Serial-to-Parallel
SIFS	Short Inter Frame Space
SISO	Single-Input Single-Output
SNR	Signal-to-Noise Ratio
TDL	Tapped-Delay Line
TDM	Time Division Multiplex
TF	Transfer Function
Tx	Transmitter
TXOP	transmission opportunity
V2I	Vehicle-to-Infrastructure
V2V	Vehicle-to-Vehicle
ZF	Zero-Forcing

Chapter 1

Introduction

1.1 Motivation and relevance

Freight traffic in California depends, to a large degree, on trucks, due to their flexibility in visit warehouses, distribution centers, and terminals. However, trucks pose major challenges to traffic and road safety. Their dynamics are slower, their inertia much higher especially when loaded, collisions involving trucks are more deadly, and in general where the flow of trucks is high (especially in the vicinity of ports), traffic congestion is more likely. For these reasons, new methods have to be found to increase the efficiency of truck transportation, and to provide better safety in an environment in which trucks and passenger cars are present in a mixed environment.

One of the most promising ways of increasing efficiency of vehicle movement is the formation of convoys. Convoys have a multitude of advantages, which can be summarized as follows:

- Vehicles can reduce wind drag, thus improving fuel efficiency, when driving together,
- A higher traffic density can be allowed without increasing probability of traffic jams with shorter inter-vehicle distances,
- The probability of accidents can be reduced when the speed of the convoy is uniform,
- The drivers are less exhausted when constant lane changes are eliminated.

For this reason, research into truck convoys, and the strongly related topics of automated vehicle control and self-driving cars has created great interest [1, 2, 3, 4, 5]. There are two forms of convoys, both of which impact mixed passenger-freight traffic:

- Pure truck convoys for freight movement, which interact with non-convoy passenger vehicles (e.g. passenger cars in front of (or behind) the truck convoy, cars in other lanes, cars merging onto the highway on which the convoy is moving, etc.),
- Mixed truck-passenger car convoys, in which vehicles with common final destinations (or at least long stretches of common routes) act as a joint convoy.

A key requirement for convoy formation is automated control of the distance between the participants. In its simplest form, this can be achieved when each vehicle is equipped with a radar that determines the distance to the preceding vehicle, which in turn serves as the major input to the control loop. However, this solution increases the danger of a “chain effect”: if a vehicle near the front of the convoy hits an obstacle, not only might the subsequent vehicle rear-end it, but each of

the subsequent vehicles will rear-end its predecessor, since it will get an indication of the changed situation only from its predecessor, and not from the front of the convoy. For this reason, communications systems that can convey information between larger groups of vehicles are essential for safety. Besides, such networks have numerous other benefits, such as communicating road conditions, traffic light status, etc. Such communications are also very helpful in the interaction with non-convoy passenger vehicles, such as announcing the length of the convoy, warning vehicles in cross-streets or on acceleration lanes of oncoming convoys, etc.

In recent years, an international standard has emerged for wireless communications between vehicles, namely the WAVE (IEEE 802.11p) standard [6]. This standard is very similar to the wildly popular IEEE 802.11a (WiFi) standard, and is supported by vehicle manufacturers from General Motors to Mercedes-Benz, as well as road operators and governments from the European Union to Japan. In the US, the Department of Transportation has initiated extensive field trials of these systems. It is therefore safe to say that any future convoying system will have an IEEE 802.11p compliant communications component to it. Moreover, note that communications via cellular connections (e.g. with each vehicle connecting to an LTE cellular base station) are not a viable alternative, due to the large latencies that data packets can experience on such connections. The similarity of the IEEE 802.11p standard to WiFi is a major strength, as it will allow the construction of very low-cost devices the economy-of-scales implicit in WiFi devices will directly translate to IEEE 802.11p. However, WiFi was designed and tested for almost-stationary applications in indoor environments, which turns out to be very different from the V2V applications. There is as of yet considerable doubt whether the IEEE 802.11p standard will work equally well, and in particular how reliable it will be under various circumstances.

In order to test its actual usability, it is required to either perform large-scale field tests with actual IEEE 802.11p compliant devices, or to alternatively develop detailed models for the propagation channel between the participating vehicles, and simulate the behavior of the IEEE 802.11p compliant nodes over such channels. The latter alternative is not only much more cost-effective, but also allows to investigate the impact of custom modifications of the standard and thus will be considered during this project. Although the performance of the IEEE 802.11p have been widely explored for V2V wireless communications between passenger cars, there are hardly any results available when both trucks and passenger cars are simultaneously on the road, i.e. between cars and trucks, and between cars whose connection is blocked by trucks.

1.2 Contributions

Motivated by the aforementioned considerations and to remedy this situation, the overall purpose of this project is to investigate the performance of IEEE 802.11p systems for interactions of convoys with mixed truck/car situations, and assess the impact on convoy formation. In particular, the main scientific contributions of this project can be summarized as follows:

- To develop equipment enabling versatile, mobile measurements of wideband propagation channels (**work package #1**). Main emphasis will be on the rapid readout of data so that a continuous streaming of the measurement results becomes possible. The outcome will be a fully functional real-time measurement platform for vehicle-to-vehicle propagation channels, which can vary very rapidly over time.

  On the other hand, antenna arrays will be designed, manufactured, evaluated and calibrated for Multiple-Input Multiple-Output (MIMO) measurements of the double-directional characteristics of the radio propagation channels,

- To perform extensive measurement campaigns of propagation channels in scenarios in which both trucks and passenger cars are on the road (**work package #2**), including *(i):* communications between adjacent trucks, *(ii):* communications between trucks separated by other trucks, *(iii):* Communications between passenger cars separated by trucks, and *(iv):* communication between a truck in a convoy on a highway, and a passenger car on an acceleration lane. These scenarios are clearly of great importance for mixed-traffic convoys, yet have scarcely been explored or measured in the existing literature.

  Note that communications between two adjacent passenger vehicles has already been investigated extensively and will thus not be specifically targeted in this project,

- To derive a model for inter-vehicular propagation channels (**work package #3**), which can be used more easily for system simulations than the "raw" measurement data. For that purpose, a Geometry-based Stochastic Channel Model (GSCM) approach will be considered, which consists in placing (diffuse or discrete) scatterers at random, according to certain statistical distributions, and assigning them (scattering) properties. The signal contributions of the scatterers are determined from a greatly-simplified ray tracing, and finally the total signal is summed up at the receiver. This modeling approach has a number of important benefits, namely *(i):* it can easily handle non-stationary channels, *(ii):* it provides not only delay and Doppler spectra, but inherently models the MIMO properties of the propagation channel, *(iii):* it is possible to easily change the antenna influence, by simply including a different antenna pattern, and *(iv):* the environment can be easily changed.

  For each scenario described in work package #2, a GSCM will therefore be developed and fully parametrized based on the corresponding measurement data,

- To create a simulation platform for the IEEE 802.11p standard (**work package #4**). It will perform a symbol-by-symbol simulation of the transmission of data packets, taking into account both the Physical Layer (PHY) and the Medium Access Control (MAC) structure of IEEE 802.11p compliant transmissions,

- To provide an evaluation framework that can assess in a reproducible way the performance of IEEE 802.11p compliant communications systems (i.e. with "standard" receivers) for mixed-traffic convoys, based on measured data (**work package #5**).

  It will tell us not only the probability of successful communication between vehicles, but also analyze robust methods such as multi-hop to resolve the situations where direct communications are not successful. The reliabilities and latencies of the wireless links thus obtained will provide critically important input for the design of control systems, and even for the development of policies and technologies for convoy formation.

This project constitutes therefore a significant and critically important contribution to the design of convoy policies, enhanced automated driver assistance, and even self-driving cars.

1.3 Outline

The remainder of this report is organized as follows: Chapter 2 presents the measurement equipment (channel sounder and antenna arrays) that we have designed, developed, manufactured and tested during this research project. In particular, we emphasize its relevance in the framework of this project when rapidly time-varying propagation channels between moving vehicles are to be measured and characterized. Chapter 3 describes the measurement campaigns that have been

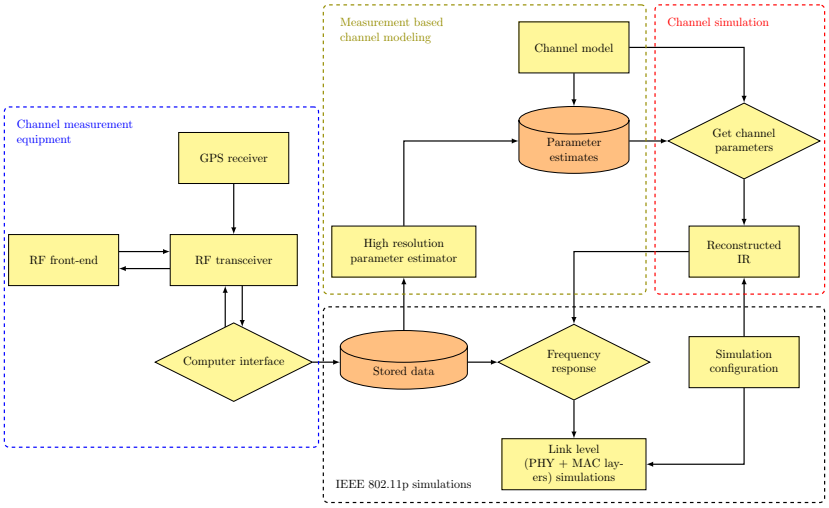

Figure 1.1: Relationships between the different tasks and work packages of the project

conducted, including the vehicles as well as the different environments and scenarios of interest. Chapter 4 outlines the channel model as well as its different components. The proposed channel model is completely parametrized from the measurements for each scenario and its implementation recipe is provided. Chapter 5 includes a detailed description of the IEEE 802.11p PHY and MAC layer models, which have been implemented in MATLAB. Results of IEEE 802.11p PHY and MAC layer simulations are presented in Chapter 6. Finally, conclusions and recommendations are discussed in Chapter 7.

Chapter 2

Construction of channel measurement test equipment

2.1 Description of the real-time MIMO channel sounder

A real-time continuous MIMO channel sounder has been completely implemented and tested during this project. It is based on the NI-USRP RIO software defined radio platform, and its architecture at the Transmitter (Tx) and Receiver (Rx) sides is given in Fig. 2.1.

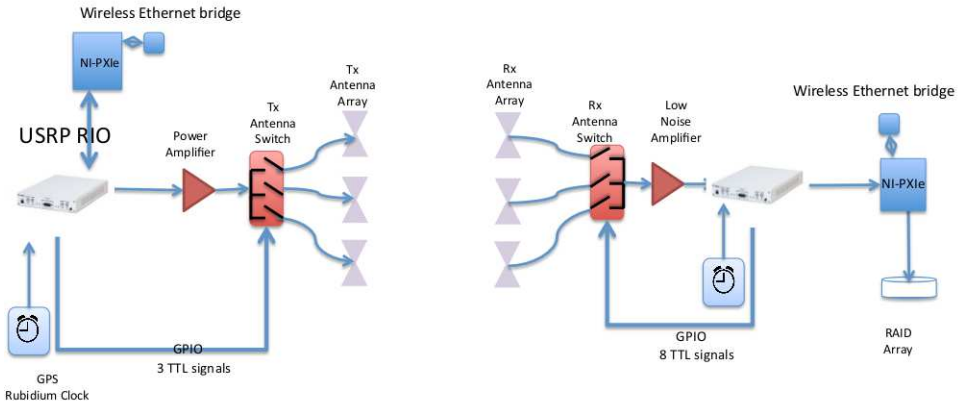

Figure 2.1: Diagram of the real-time MIMO channel sounder at the transmitter (left) and receiver (right) sides, respectively

The channel sounder performs switched-array MIMO measurements. It transmits a Orthogonal Frequency Division Multiplexing (OFDM)-like sounding signal around 5.9 GHz with a bandwidth of 15 MHz. The output power is about 26 dBm. Since the NI-USRP RIO platform uses a direct up-conversion (DUC) architecture, we implement the intermediate frequency (IF) sampling for both the Tx and the Rx, so that we minimize the negative effects of the DC offset problem that usually bothers wireless transceivers with DUC architectures. The frequency of the Local Oscillator (LO) is 5.888 GHz, which is 12 MHz smaller than the center frequency of the sounding signal.

The two USRPs are synchronized with two GPS-disciplined rubidium clocks. The rubidium clocks provide 1 Pulse Per Second (PPS) for absolute time synchronization, and 10 MHz as the reference clock for the timing modules on two USRPs. It is noteworthy that the 10 MHz reference clock is further utilized by the USRPs to derive the FPGA data clocks (40 MHz, 120 MHz) as

Parameter	Value
Carrier frequency	5.9 GHz
Bandwidth	15 MHz
Transmit power	26 dBm
Sampling rate	20 MS/s
MIMO signal duration	$640\mu s$
Number of MIMO per burst	30
Rate of bursts	20 Hz
Number of bits in ADC	16

Table 2.1: Parameters of the real-time MIMO channel sounder

well as the LO. The USRP-RIO 2953R runs with two 16-bit ADCs for both I and Q channels. When sampling at 20 MS/s, the output data rate is around 80 MBps with a full duty cycle. Tab. 2.1 provides a detailed list of parameters of the channel sounder.

2.1.1 Implementation details of the channel sounder

To fully control USRPs in the channel measurement, we have written customized codes in LabView and LabView FPGA. We have started from the USRP streaming sample project, added additional controllers and made necessary modifications. The diagram of the LabView script for the Rx USRP is given in Fig. 2.2, where the red block is further detailed in Fig. 2.3.

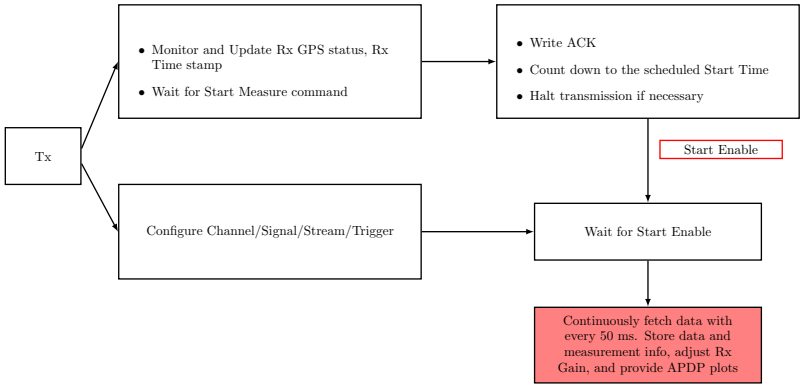

Figure 2.2: Functionality diagram of the Rx USRP

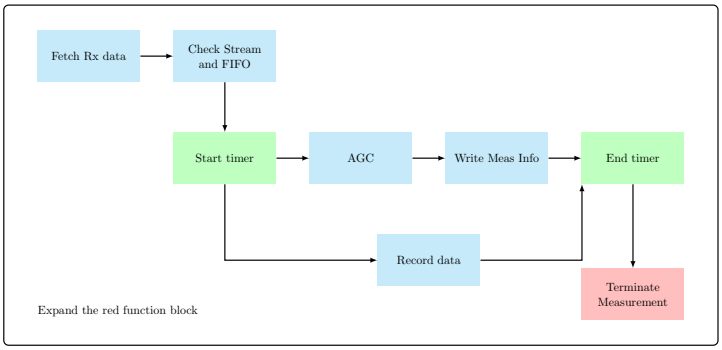

Figure 2.3: Functionality diagram of the main loop of continuous sampling at the Rx USRP

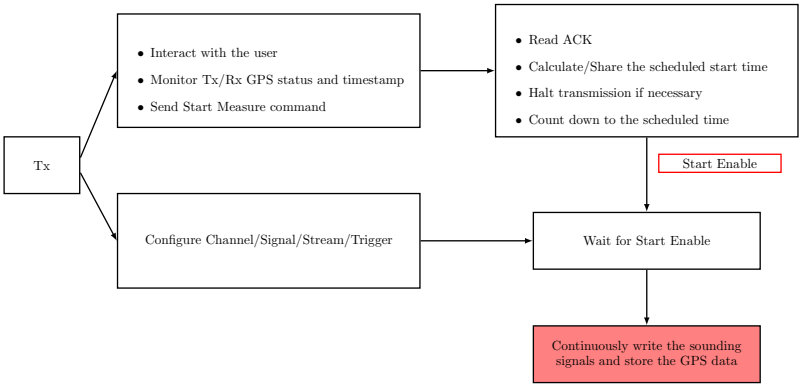

Figure 2.4: Functionality diagram of the Tx USRP

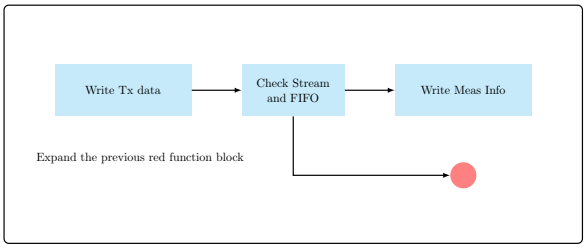

Figure 2.5: Functionality diagram of the main loop of continuous sampling at the Tx USRP

Fig. 2.4 gives the functionality diagram of the LabView script for Tx USRP. Fig. 2.5 expands the contents of the red function block in Fig. 2.4. The continuous streaming between Tx and Rx USRPs are initiated by software triggers from separate host PCs. These two triggers are buffered by the FPGA and synchronized to the rising edge of external PPS signals from two GPS-disciplined Rubidium clocks. Though the rising edge of the PPS signal is aligned to UTC time and has small jitters, it still has a standard deviation of 3.3 ns when locked. Hence it is crucial that we avoid repeated triggers during the continuous streaming to preserve the phase coherence in MIMO channel measurements, what is essential for high-resolution parameter extraction algorithms such as RiMAX [7] and EKF [8].

The MIMO sounding signal frame structure consists of 8×8 elementary sounding signals, as shown in Fig. 2.6. Several guard periods are needed in-between these sounding signals in order to allow the settling time of the Tx and Rx switches. The related parameters are summarized in Tab. 2.2. Note that with these settings, the maximum resolvable Doppler shift is equal to $\nu_{max} = 1/(2T_0) = 806$ Hz, which yields a maximum relative speed between the Tx and Rx vehicles and the discrete scatterers of $\Delta v_{rel,max} \approx 148$ km/h. In other words, measurement data will suffer from Doppler ambiguities (or, equivalently, the temporal behavior of the corresponding fading process will be undersampled) whenever $\Delta v_{rel,max} > 148$ km/h. This phenomenon can typically occur in highway environments for scatterers traveling with high velocities in a direction opposite to the one of the Tx and Rx vehicles.

2.1.2 Back-to-back system calibration

The back-to-back system calibration is performed by making a cable connection between Tx USRP and Rx USRP. Radio-Frequency (RF) attenuators are also used in-between in order to ensure the safety of the Rx USRP. We have made continuous streaming measurements with the set-up, so we can average over multiple realizations to further improve the Signal-to-Noise Ra-

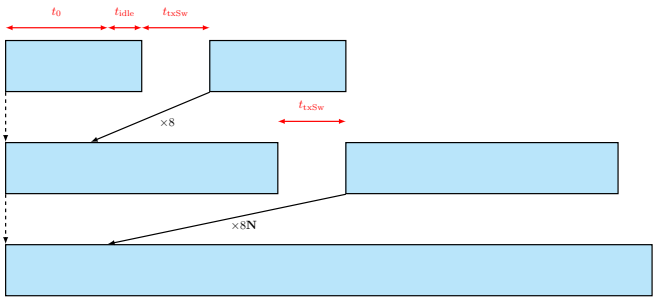

Figure 2.6: Frame structure of MIMO sounding signal

Parameter	Definition	Value
t_0	Unit signal	$4\mu s$
t_{idle}	Unit signal buffer	$4\mu s$
t_{rxSw}	Guard time for Rx switch	$0.5\mu s$
t_{txSw}	Guard time for Tx switch	$10\mu s$
T_0	MIMO snapshot duration	$620\mu s$
N	Repetition of MIMO snapshot	30

Table 2.2: Parameters of the MIMO sounding signal

tio (SNR) of the system calibration data, i.e.

$$Y_{\text{REF}}(f) = \mathbf{E}\{Y(f)\}, \tag{2.1}$$

where $Y_{\text{REF}}(f)$ is our final system calibration result and depends on the gain setting of the Rx USRP. It is intended for the pre-processing of the measurement data, which is given by

$$H(f) = \frac{Y_{\text{MEAS}}(f)}{Y_{\text{REF}}(f)} \cdot G_{\text{ATTEN}}(f), \tag{2.2}$$

where $H(f)$ is the channel Transfer Function (TF), whereas $G_{\text{ATTEN}}(f)$ is the transfer function of the attenuator used during the back-to-back system calibration. Note that $H(f)$ can be directly used as such for RiMAX evaluation. Since we use a cable with attenuators, the repeated measurements also reflect the stability of the channel sounder. All TFs from different Single-Input Single-Output (SISO) snapshots are normalized with respect to the first one, which is given by

$$X_f^{\text{rel}}(f, m_r, m_t, t, ix) = \frac{X_f(f, m_r, m_t, t, ix)}{X_f(f, 1, 1, 1, 1)}. \tag{2.3}$$

By assuming that the variations within one SISO snapshot are negligible, the average relative TF can then be expressed as

$$\bar{X}_f^{\text{rel}}(m_r, m_t, t, ix) = \mathbf{E}_f\{X_f^{\text{rel}}(f, m_r, m_t, t, ix)\} \tag{2.4}$$

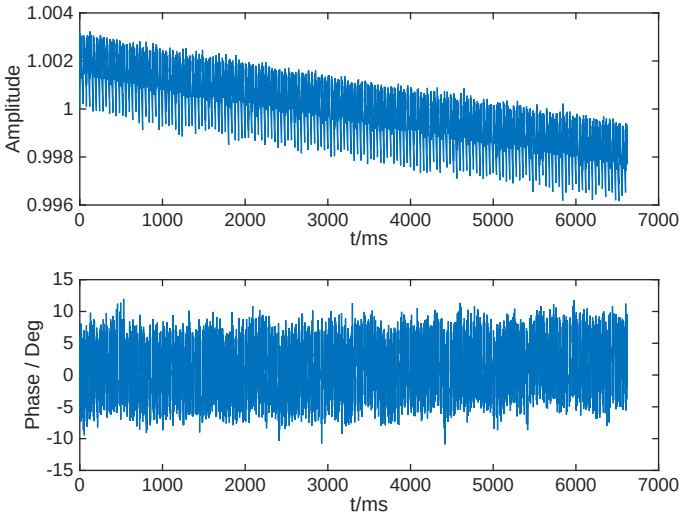

Figure 2.7: Amplitude and phase variations of USRP channel sounder, when using a common GPS-disciplined rubidium clock: $\sigma_{pn} = 2.47^o$, LO frequency is 5.888 GHz

2.2 Multi-antenna arrays

2.2.1 Antenna array design

We have decided to build two 8-element vertically polarized uniform circular dipole arrays (VP-UCDA) for our V2V measurement campaigns. In order to hold the antenna arrays firmly during the measurements, we have also customized and built two array stands with the aid from the USC Machine Shop. The stand is made of two plates and one pillar, and antennas were soldered and mounted close to the middle section of the pillar. The stand is also equipped with clamps on the bottom so that the entire structure is able to stick with a cargo basket on the roof top of the vehicles (passenger cars or trucks). A picture of the stand can be found in Fig. 2.8.

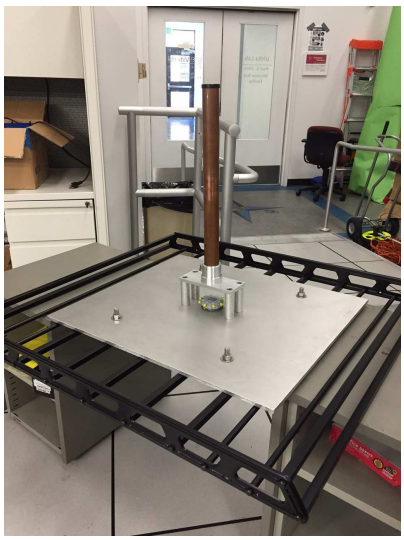

Figure 2.8: Array stand with its metallic base

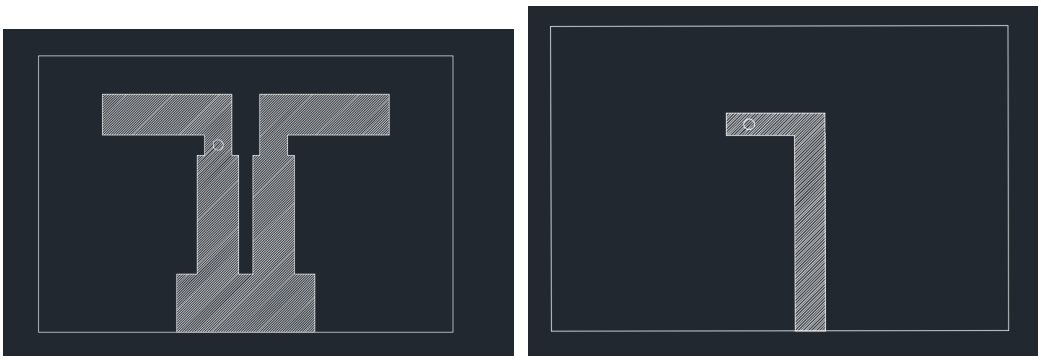

(a) Top (b) Bottom

Figure 2.9: Etch Layers of the dipole antenna

Similar to the array introduced in [9], all the half-wavelength dipoles are mounted in the middle of a cylindrical metallic pillar that serves as a ground plate. The metallic pillar not only increases the directivity of each dipole antenna in the direction that it is facing, but also reduces the mutual coupling between antenna elements. For the design of the antenna elements, at the beginning we tried to use the cylindrical dipole with a quarter-wave balun feed that is introduced in [10]. But the small dimensions of the antenna made it extremely difficult for us to build it. We have therefore decided to use dipole antennas on printed circuit boards introduced in [11]. The final design of the printed dipole antenna is optimized through the electromagnetic simulation software CST [12], and is illustrated in Figs. 2.9(a) and 2.9(b). The simulated far-field antenna pattern at 5.9 GHz is provided in Fig. 2.10.

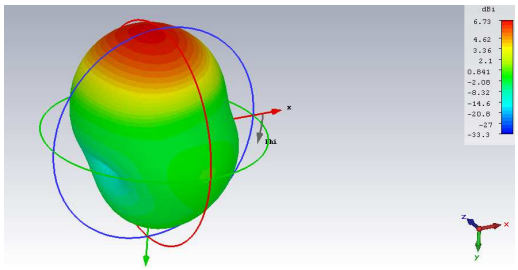

Figure 2.10: Simulated far-field pattern of the dipole antenna at 5.9 GHz

2.2.2 Antenna array calibration

Array calibration with high quality is important for any high-resolution parameter extraction algorithm. The characterization of the response of the antenna array together with the RF switch needs therefore to be done in an anechoic chamber.

The calibration data s_{21} is a 3D complex tensor. It is denoted by $s_{21}(f, \varphi, i)$, where f is the frequency index, φ is the azimuth angle, and i is the antenna index, respectively. The discrete version is given by

$$s_{21} \in \mathbb{C}^{N_f \times N_{az} \times M_{ant}}, \tag{2.5}$$

where N_f, N_{az} and M_{ant} are the number of frequency points, azimuth angles and antennas, respectively. It is *important* to realize that the original calibration data is corrupted with measure-

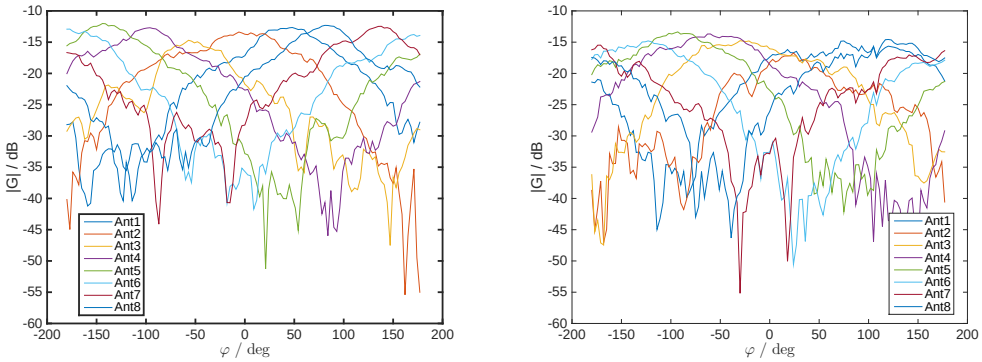

(a) Rx antenna array

(b) Tx antenna array

Figure 2.11: Radiation patterns of the antenna array elements, calibrated with the corresponding RF switch

ment noise as well. The typical data processing from the original s_{21} to the array complex beam pattern follows

$$B\left(\varphi, i\right) = \mathbf{E}_f\left\{G_{\text{ANT}}\left(f, \varphi, i\right)\right\} = \mathbf{E}_f\left\{\frac{s_{21}\left(f, \varphi, i\right)}{G_{\text{REF}} \cdot H_{\text{free}}\left(f\right)}\right\}, \tag{2.6}$$

where the expectation operation $\mathbf{E}\{\cdot\}$ performs over various frequency points. The free-space Line-Of-Sight (LOS) channel transfer function is determined by

$$H_{\text{free}}\left(f\right) = \frac{1}{\sqrt{4\pi d^2}} e^{-j2\pi f d/c_0}, \tag{2.7}$$

where d is the distance between the reference antenna and antenna under test in the calibration. We use those angular points among the calibration data s_{21} that have sufficiently high amplitude (-53 dB). The calibration distance is estimated from the gradient of the phase versus frequency, such that

$$d = \frac{-1}{2\pi} \frac{\mathrm{d}\phi\left(f\right)}{\mathrm{d}f}. \tag{2.8}$$

The vertically polarized pattern of each element of the Rx and Tx antenna arrays is given in Figs. 2.11(a) and 2.11(b), respectively. The 2D ambiguity function of Rx array is shown in Fig. 2.12. The high ridge lies along the diagonal as expected in Fig. 2.12. Moreover, the array response was further tested with synthetic channel Impulse Responses (IRs), which were evaluated using the high-resolution parameter estimation algorithm 4D-RiMAX (described later in Chapter 4). The initial estimation results indicate that the parameters of simulated Multipath Components (MPCs) can be successfully recovered.

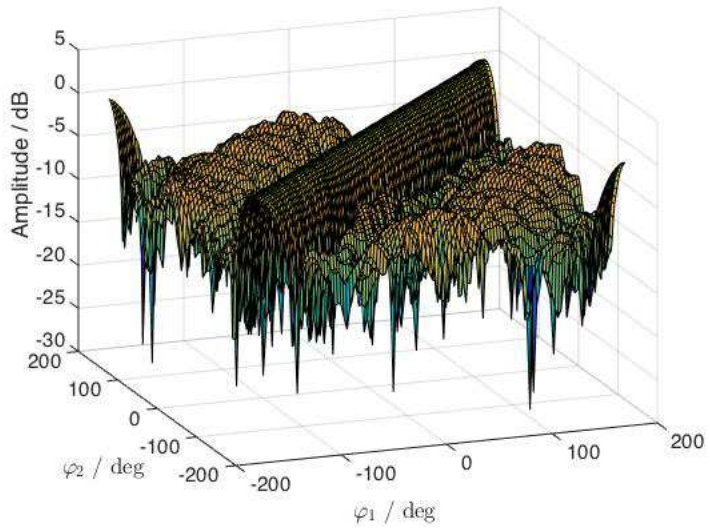

Figure 2.12: 2D ambiguity function of the Rx antenna array

Chapter 3

Channel measurement campaigns

The characteristics of vehicular propagation channels depend intrinsically on the nature of the surrounding environment. For this reason, vehicular measurement campaigns have been carried out in various propagation environments, e.g. [13, 14, 15, 16, 17, 18]. The campaigns are conducted for V2V scenarios, by letting two vehicles drive in convoy or in opposite directions while measuring, or for Vehicle-to-Infrastructure (V2I) scenarios which can be emulated by parking one of the vehicles. The most common environments, i.e. urban, suburban, highway and rural, have also been widely investigated for cellular systems. Other campaigns concentrate on specific scenarios such as intersection collision avoidance and co-operative merging assistance [19, 20, 21].

Since a key goal of the inter-convoy communication is to convey information between widely separated vehicles, the shadowing of the transmitted signal by vehicles between the Tx and Rx ones is of special importance. In particular, communications between two passenger cars between which a truck is located can easily suffer from a blocked LOS. Despite this importance, there are hardly any relevant measurements of this effect. Previous experimental papers about large vehicle obstructions investigate the blockage effect of a large box truck passing through the LOS path at 11 GHz [22], or the obstructions of multiple vehicles between Tx and Rx on path loss model at 60 GHz [23]. However, due to the use of different frequency bands (5.8 GHz for IEEE 802.11p), these results cannot be used for the typical V2V applications. Moreover, the Non-Line-of-Sight (NLOS) cases caused by the vehicles in [24] and [25] either include the effect of the small cars and vans, or occur intermittently in the measurements. As a result, those results cannot fully reflect the impact of large vehicle obstructions on the propagation channels. In [26], the effect of the trucks and vans on the received signal strength is investigated. Most of the measurements are conducted at several separate locations, so that the discontinuous (with respect to distance) sampling complicates a detailed and accurate analysis of shadow fading. In other words, the design and deployment of IEEE 802.11p compliant communication systems for the specific case of mixed truck/passenger vehicle convoys requires the extensive evaluation of the underlying radio propagation channels in real-world scenarios. However, there is to date hardly any dedicated measurement campaign for the characterization of *(i):* the propagation channel for truck-to-vehicle or truck-to-truck communications and *(ii):* how different the propagation channel is when the antennas are mounted on top of the driver cabin.

In order to fill this gap, an extensive measurement campaign has been conducted in April 2016 using the equipment set-up described in Chapter 2, with two major objectives in mind:

- Measuring truck-to-vehicle and truck-to-truck propagation channels in various scenarios and environments. Then, based on the collected data, accurate (fully parametrized) channel models are established and the performance of IEEE 802.11p compliant communication

systems in these situations are assessed,

- Analyzing the impact of the Tx and/or Rx truck trailer(s) as well as of other truck(s) as obstructing vehicle(s) in a systematic and controlled fashion.

In this Chapter, we discuss the main characteristics of the measurement campaign, along with the scenario and environment descriptions. The so-collected measurement data will serve as a basis for the analysis conducted in the next Chapters.

3.1 Measurement vehicles

3.1.1 Passenger cars

In order to perform a realistic characterization of the propagation channel, two standard passenger cars were used at the Tx and Rx sides during the measurements, i.e. *(i):* a Dodge Journey Mid-size cross-over sport Utility SUV, and *(ii):* Hyundai Sante Fe Mid-size SUV, as shown in Fig. 3.1. The Dodge Journey has dimensions of 4.88 m in length, 1.83 m in width and 1.69 m in height, whereas the dimensions of the Hyundai Sante Fe are 4.5 m in length, 1.84 m in width and 1.67 m in height.

(a) Hyundai Sante Fe SUV (b) Dodge Journey SUV

Figure 3.1: Photos of the SUVs used as our test vehicles

The sounder and the batteries needed for power supply were assembled in two separate server racks (Tx, Rx), as shown in Fig. 3.2(a) and 3.2(b). They are stored in the trunk and on the back seats of the cars and trucks, as shown in Fig. 3.2(c). On the other hand, the Tx and Rx antenna arrays were mounted on a basket attached in the center of the car rooftops using ski racks, as shown in Fig. 3.3. They are connected to the measurement equipment inside the cars through RF cables running through door windows on the passenger side. Throughout various measurement campaigns, we make sure the azimuth angle 0°defined for the antenna array is aligned with the front direction of the vehicle.

3.1.2 Trucks

For the two trucks involved in the car-to-truck and truck-to-truck channel measurements, we have rented two 16 foot studio trucks from Ryder. Fig. 3.4(a) provides a side view of the studio truck. It has a load capacity of 6000 lbs and up to 960 cube feet of cargo space. The main reasons this type of truck was considered are that *(i):* it provides sufficient space in the driving cabin to allow the placement of the channel sounder, and *(ii):* its flat roof is also able to accommodate the installation of metallic basket and antenna array, as shown in Fig. 3.4(b).

(a) At the Tx side (b) At the Rx side (c) Tx server rack in the back seats of the truck

Figure 3.2: Photos of the server racks holding the equipment

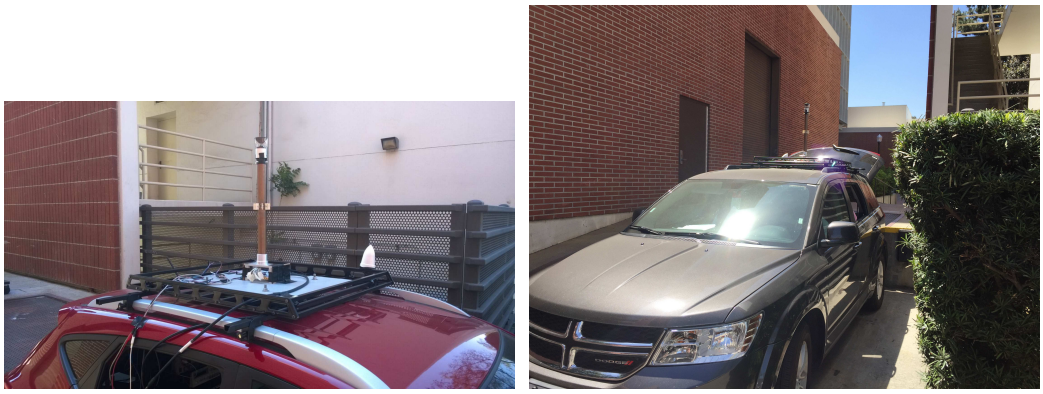

(a) At the Tx side (b) At the Rx side

Figure 3.3: Photos of the antenna arrays on top of the SUVs

3.2 Mixed-traffic scenarios

A number of important situations for mixed truck/passenger car traffic have been identified, in terms of both road safety applications and convoy formation efficiency. With these applications in mind, a number of scenarios have been investigated, including

- *Communications between adjacent trucks*: The most straightforward scenario is the communication between two trucks that are following each other in the convoy. Despite the fact that this is an obviously important scenario, hardly any measurements of associated communications channels exist. The placement of the antennas on the roof of the driver cabin has a major impact on the results, owing to the material and height of the trailer. It results in either a large pathloss/shadowing of the LOS component if the Tx and Rx trucks are travel-

(a) Side view of the truck (b) Tx antenna array on top of the truck

Figure 3.4: Photos of the 16 foot studio truck used as our test vehicles

ing in the same direction (even with no other vehicle in-between them), or a strong reflected contribution if the two vehicles are traveling in opposite directions,

- *Communications between trucks separated by other trucks*: If one of more trucks are between the Tx and Rx ones, they will shadow off some of the signals that would normally reach the Rx. If all trucks are of identical make, we can expect from diffraction theory that the additional pathloss will be about $3-6$ dB per truck, plus the pathloss associated with the larger spacing between the Tx and Rx trucks. However, for trucks with varying height and different shape of the trailers, larger pathloss/shadowing might occur,

- *Communications between passenger cars separated by trucks*: If trucks separate transmitters and receivers located on passenger cars, the shadowing effect can be significantly more pronounced than for transmitters and receivers located on trucks themselves. This is due to the fact that the height of the antennas is much lower when mounted on a passenger car, and the relatively large diffraction angles create a stronger attenuation. In our recent preliminary work [27], we have investigated the channel between two passenger cars separated by a school bus, and found more than 10 dB attenuation (as well as a significant change of the dispersion characteristics). Furthermore, for such a scenario, the surrounding environment might play a significant role. For example, in a street canyon, signals might mostly propagate from the transmitter via reflection on a house wall to the receiver, thus reducing the importance of the diffraction over the top of the truck. On the other hand, such a signal path will not be available in an open (rural) area.

- *Communication between a truck in a convoy on a highway, and a passenger car on an acceleration lane*: This scenario is also of obvious practical importance for the interaction between freight and passenger traffic.

Note that communications between two adjacent passenger vehicles have already been investigated extensively (among others by us) and will thus not be specifically targeted in this project.

3.3 Environments

For each of the aforementioned scenarios, appropriate measurement sites were carefully selected, so that generalized conclusions can be drawn. All the measurement sites are located in and around

Los Angeles (CA, USA). For each scenario, measurement runs were taken continuously "on the fly" and consist of typically $5 - 20$ minutes of recorded data, i.e. significant enough for the estimation of meaningful and reliable statistics. In the following, the investigated environments are discussed in detail.

3.3.1 Urban areas

Measurements were performed in DTLA, i.e. a densely populated area with single- to multi-story buildings lined on both sides of the road. Streets are $15 - 40$ m wide, multi-lane and mostly one-way, organized according to a grid system (i.e. with right-angle street intersections), as shown in Fig. 3.5.

(a) Street canyon in DTLA

(b) Truck-to-truck convoy scenario

(c) Two trucks in opposite directions at an intersection

Figure 3.5: Different scenarios in an urban environment, in Downtown Los Angeles (DTLA)

The Tx and Rx vehicles were driven along different streets, as shown in Fig. 3.6 for one particular measurement route, at varying speeds between 0 and 14 m/s under realistic traffic conditions (red-lights, road works, light to heavy vehicle flow, etc.). Two different driving patterns have been considered in this environment, namely

- *Urban - convoy*: Both the Tx and Rx vehicles are traveling in a convoy fashion (i.e. one behind the other). The distance between the Tx and Rx vehicles was always $5 - 250$ m, hence allowing other vehicles to move between the Tx and Rx vehicles,
- *Urban - opposite*: Both the Tx and Rx vehicles are traveling in opposite directions on parallel lanes: they are first approaching each other, are then passing each other and are finally moving away from each other. In some cases, one of the vehicles is parked on the curbside while the other vehicle is traveling away from it in the same street.

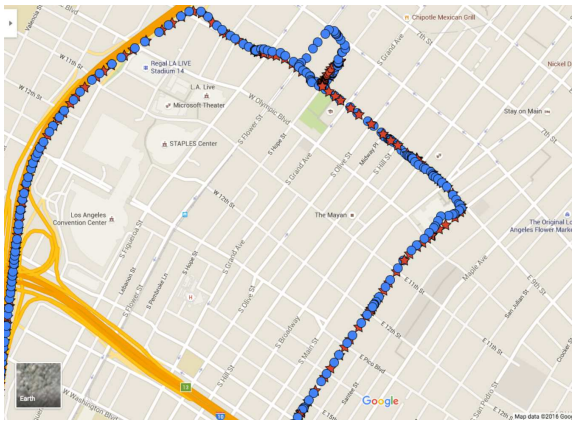

Figure 3.6: GPS locations of Tx and Rx vehicles during the channel measurements in downtown Los Angeles: blue dots are positions of Tx and red stars are positions of Rx

3.3.2 Suburban areas

Measurements were conducted in a suburban environment located around the USC campus in Los Angeles (CA, USA), which mostly consists of open areas with small detached houses and significant vegetation, as shown in Fig. 3.7. Streets are typically $10 - 30$ m wide, multi-lane with either one or two driving directions. They are also characterized by large sidewalks and road signs which are sparsely distributed.

(a) Suburban environment near the USC campus

(b) Truck-to-truck convoy scenario

(c) Truck-to-car convoy scenario

Figure 3.7: Different scenarios in an suburban environment, near the USC campus

The Tx and Rx vehicles were driven along different streets, as shown in Fig. 3.8 for one particular measurement route, at varying speeds between 0 and 14 m/s under realistic traffic conditions

(little to average traffic conditions). As for the urban environment in Section 3.3.1, two different driving patterns have been considered here, namely

- *Suburban - convoy*: Both the Tx and Rx vehicles are traveling in a convoy fashion (i.e. one behind the other). The distance between the Tx and Rx vehicles was always $5 - 250$ m, hence allowing other vehicles to move between the Tx and Rx vehicles,

- *Suburban - opposite*: Both the Tx and Rx vehicles are traveling in opposite directions on parallel lanes: they are first approaching each other, are then passing each other and are finally moving away from each other. In some cases, one of the vehicles is parked on the curbside while the other vehicle is traveling away from it in the same street.

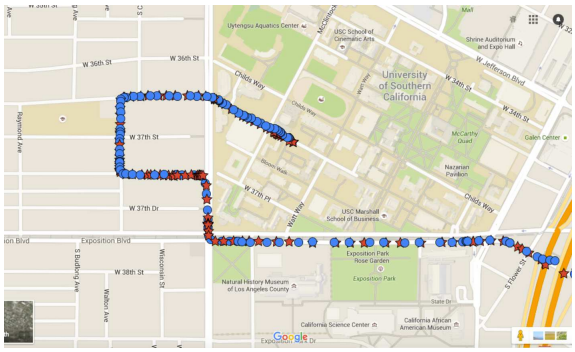

Figure 3.8: GPS locations of the Tx and Rx vehicles in a suburban environment: blue dots are positions of Tx and red stars are positions of Rx

3.3.3 Highway/Freeway areas

Measurements were conducted on highways with $2-4$ lanes in each driving direction, with sparse buildings and vegetation on either road side. The outer boundary of the road is guarded by concrete walls or sound barriers, whereas each direction of travel on the highway is separated by a metallic rail approximately 0.50 m tall. Moreover, the road is often found to be overpassed by road signs and concrete bridges, as typically shown in Figs. 3.9(a) and 3.9(b).

The Tx and Rx vehicles were traveling at a speed of $20 - 30$ m/s under realistic traffic conditions (light to congested vehicle flow, etc.) Two different situations have been considered in this environment, namely

- *Highway - convoy*: Both the Tx and Rx vehicles are traveling in a convoy fashion. The distance between the Tx and Rx vehicles ranged from 5 to 350 m, hence allowing other vehicles to move between the Tx and Rx vehicles. Measurements while overtaking or being overtaken by other vehicle were also performed,

- *Highway - merging lane*: Either the Tx or the Rx vehicle is traveling on an entrance or an exit ramp (i.e. a road merging two traffic flows into a single one), whereas the other vehicle is traveling on the highway. An important aspect here is the possibility of the LOS component being obstructed due to the slope of the ramp and the orientation of the terrain, as shown in Fig. 3.9(c). Another possible case is when both the Tx and Rx vehicles are traveling at the same time on an entrance or an exit ramp.

(a) Open I110N freeway area

(b) I110N freeway area with architectural structures (e.g. bridges, overpasses, etc.)

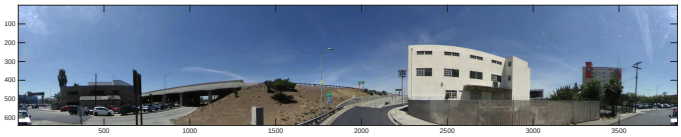

(c) Merging ramp at the entrance of I110N freeway

Figure 3.9: Different scenarios in a highway/freeway environment, in Los Angeles

3.3.4 Intersections

Measurements were conducted at street intersections in urban and suburban environments, when the Tx and Rx vehicles are approaching the road crossing from perpendicular directions. In that case, the LOS can be obstructed for long time durations when the Tx and Rx vehicles are traveling toward the intersection, owing to buildings located at the corner of the intersection, and be cleared only when both meet there. The reliability of the link between the Tx and Rx vehicles depends therefore on the availability of other scattering objects in the surrounding environment, e.g. other nearby buildings, vegetation, street signs, parked vehicles, etc. Two different cases were investigated for this scenario, namely

- *Urban, multiple lanes:* The environment consists in that case in a street intersection in the DTLA urban environment, as previously described in Section 3.3.1. Each street has two or more lanes, with only one driving direction. There are traffic lights, busy traffic, and multi-story buildings at each corner of the intersection which can either block the LOS or act as scatterers, as shown in Fig. 3.10(a),
- *Suburban, multiple lanes:* This environment consists in a street intersection in the suburban environment around USC campus, as previously described in Section 3.3.2. It is characterized by few to no buildings next to the street intersection, but an open surrounding with vegetation, small detached houses and little traffic, as shown in Fig. 3.10(b). Moreover, no severe obstruction of the LOS is experienced in that case.

3.4 Route documentation

Two 360°panoramic video cameras were positioned on top of the pillar of the Tx and Rx antenna arrays during the measurements, in order to document the scenarios and routes (traffic conditions,

(a) Urban environment, in downtown Los Angeles

(b) Suburban environment, close to the USC campus

Figure 3.10: Road intersections in different environments

environment, weather, etc.) as "seen" from the top of the truck driver cabin or passenger car rooftop, as close as possible from the antenna array elements.

Global Positioning System (GPS) coordinates of the Tx and Rx vehicles were also available directly from the channel sounder, recorded 20 times per second, hence providing a real-time display of the Tx and Rx vehicles as well as their actual instantaneous speeds during the measurements. These GPS data can be used in combination to the video recordings in the post-processing of the measurement data in order to relate estimated results (channel parameter estimation, system performance, etc.) to the physical environment surrounding the Tx and Rx vehicles, e.g. traffic conditions, number of pedestrians, houses and road side, etc.

In each vehicle, one person acted as driver, a second one operated the measurement equipment, whereas a third assisted the driver as co-pilot, was responsible for measurement documentation and communicated through mobile phones with the other vehicle in order to synchronize the traveling of the Tx and Rx vehicles one relative to the other.

3.5 Measured data

At the output of the measurement equipment, we obtain $M_R \times M_T = 8 \times 8$ complex MIMO time-varying channel TFs $\mathbf{H}(f,t)$ over a 15 MHz bandwidth centered at 5.9 GHz, see Table 2.1 for further details of the measurement parameters.

The measurement time duration was set at the beginning at each measurement session to 1 hour, meaning that the data were collected continuously "on the fly" while the Tx and Rx vehicles were traveling. The sections of measurement data most relevant to the analysis and characterization of the scenarios of interest have been carefully identified and labeled during the post-processing, in order to create a comprehensive data base.

During these measurement campaigns, we have collected over 720000 MIMO snapshots for car-to-car measurements, and over 2.5 million MIMO snapshots separately for truck-to-car and truck-to-truck measurements, respectively.

Chapter 4

Channel modeling

From the measurements presented in Chapter 3, we derive a channel model that can be used more easily for system simulations than the "raw" measurement data.

Following our previous work [28], we employ a measurement-based GSCM approach, which builds on placing (diffuse or discrete) scatterers at random, according to certain statistical distributions, in physically realistic positions in the surrounding environment (e.g. buildings on the road sides, other vehicles on the road, etc.), and assigning them (scattering) properties. The signal contributions of the scatterers are then determined from a greatly-simplified ray tracing and the total signal is finally summed up at the Rx side. This modeling approach has a number of important benefits, e.g. *(i):* it can easily handle non-stationary channels, *(ii):* it provides not only delay and Doppler spectra, but inherently models the MIMO properties of the channel, *(iii):* it is possible to easily change the antenna influence, by simply including a different antenna pattern, and *(iv):* the environment can be easily changed.

The remainder of this Chapter is structured as follows: in Section 4.1, we use a high-resolution method (RiMAX) that allows extracting the parameters of the discrete scattering contributions from the IRs for each MIMO burst. Then, in Section 4.2, the discrete scatterer contributions are tracked over large distances, based on the so-obtained parameters. Section 4.3 introduces the general outline of the generic GSCM approach in vehicular environments, including a detailed description of its main characteristics (i.e. environment geometry, discrete and diffuse scattering). Finally, Section 4.4 provides the complete parametrization of the propagation channel model, which is validated by comparing the simulated Root Mean Square (RMS) delay spread to the one estimated from the measured data.

4.1 Parameter estimation

4.1.1 Overview

A full parametrization of a channel model demands efficient and robust parameter estimates , which can be obtained from multidimensional channel measurements. The data is usually captured by a sophisticated channel sounder equipped with multiple antenna arrays, and further evaluated with high-resolution parameter estimation algorithms. Different from classical non-parametric approach, these algorithms greatly enhance the resolution and accuracy by fitting an appropriate data model to the measurement data. RiMAX is one of these high-resolution parameter estimation algorithms and is based on a joint Maximum Likelihood Estimator (MLE) for both concentrated discrete scatterer contributions and Diffuse Multipath Component (DMC) for wireless MIMO channel measurements [29].

Compared with the now well-known Space-Alternating Generalized Expectation-Maximization (SAGE) algorithm [30], RiMAX has a more complete data model and a much faster convergence rate for the iterative estimation. It applies a data model that accounts for contributions from both discrete scatterer contributions as well as DMC in the wireless medium. Overlooking the DMC in the data evaluation (as it is the case in SAGE) usually leads to an over-fitting of the estimation problem [31] and an underestimation of the channel capacity [32]. Meanwhile, the convergence rate of SAGE drops significantly when the sources are coupled, i.e. when the parameters of the discrete scatterer contributions are close to each other: this limits the effectiveness of SAGE in evaluation on real propagation channel data, since it is quite often to see cluster of discrete scatterer contributions (correlated sources) in the wireless channel. On the other hand, RiMAX circumvents this problem by numerically solving a joint optimization of all concentrated discrete scatterer contributions.

We have mainly followed the framework in [29] and extended its application to V2V channel measurements. Particularly the data model applied in our proposed algorithm emphasize the inclusion of the Doppler shifts of specular paths (SPs), since V2V wireless propagation channels can be highly dynamic and produce large Doppler spreads. In this case the phase rotation due to the Doppler shift is no longer negligible within one MIMO snapshot for our channel sounder described in Chapter 2. Following the accelerated parameter initialization method in [33], we have developed a similar initialization algorithm for V2V application. It is noteworthy that though this adopted data model was first suggested in [29], to the best of our knowledge, neither implementation details nor exemplary applications of this data model are available in the open literature.

4.1.2 Introduction to the RiMAX algorithm

The propagation channel measurement data consists of contributions from concentrated SPs, DMC and noise. Assuming the number of observable specular paths is P, the propagation channel observation vector, denoted by $\mathbf{x}$, can be expressed as

$$\begin{aligned}\mathbf{x} &= \sum_{p=1}^{P} \mathbf{s}(\theta_{sp,p}) + \sqrt{\alpha_0}\mathbf{w} + \mathbf{n}_{dmc} \\ &= \sum_{p=1}^{P} \mathbf{s}(\theta_{sp,p}) + \mathbf{n}_{dan}. \end{aligned} \tag{4.1}$$

For clarity, we combine the vector $\sqrt{\alpha_0}$ describing the measurement noise and the DMC contribution to the observation in one vector $\mathbf{n}_{dan} = \mathbf{n}_{dmc} + \sqrt{\alpha_0}\mathbf{w}$. Both the measurement noise and the DMC are assumed to be circular complex Gaussian processes. The MLE is then given by

$$\hat{\theta} = \arg \max_{\theta} p(\mathbf{x}, \theta). \tag{4.2}$$

Assuming no prior information about $p(\theta)$, we have

$$\hat{\theta} = \arg \max_{\theta} p(\mathbf{x}|\theta). \tag{4.3}$$

By separating the parameters into those related to concentrated SPs and those of DMC, this relationship can then be rewritten as

$$\begin{bmatrix} \hat{\theta}_{sp} \\ \hat{\theta}_{dan} \end{bmatrix} = \arg \max_{\theta_{sp},\theta_{dan}} \left\{ \frac{1}{\pi^M \det(\mathbf{R}(\theta_{dan}))} e^{-(\mathbf{x}-s(\theta_{sp}))^H \mathbf{R}^{-1}(\mathbf{x}-s(\theta_{sp}))} \right\}. \tag{4.4}$$

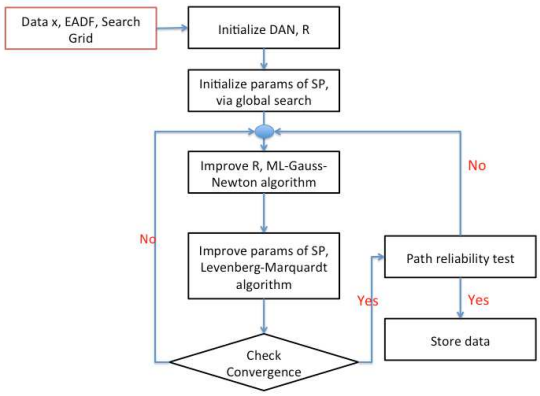

Figure 4.1: RiMAX code flow

The above optimization problem can be solved by choosing parameter subsets and maximizing the objective function in an alternating manner. The obvious choice for the two parameter subsets are the SP and DMC ones, i.e. $\hat{\theta}_{sp}$ and $\hat{\theta}_{dan}$, respectively.

The code flow of the RiMAX algorithm is shown in Fig. 4.1: for the first phase of RiMAX, it finds initial estimates for both the DMC and the SPs. Strong SPs are firstly removed from the observation vector and fed into an iterative estimator for the DMC and noise processes [34], and we obtain an initial estimate for the covariance matrix of the stochastic part of the measured channel. The SPs are then detected and estimated sequentially via a grid-based multidimensional search[1]. In the second phase, updates on the estimates for the SP and the DMC processes are carried out alternatively and iteratively. Basically the joint optimization problem is split to two sub-problems, one is a deterministic maximum likelihood (DML) problem for the SPs and the other is a stochastic maximum likelihood (SML) for the DMC and the measurement noise. The two optimization problems are solved numerically with gradient-base algorithms, such as Levenberg-Marquardt algorithm and Gauss-Newton algorithm. The "raw" estimates from the first phase are used as the initial values in the iterative optimization algorithm. After convergence, the refined estimates are passed on to a path reliability test, where the SPs with high estimation variance are dropped. The number of SPs can therefore be adjusted in this test. If all the SPs pass the test, RiMAX stores the final results.

4.1.3 Signal data model

In this section, we introduce the details of our novel signal model for specular paths in the wireless channel measurements. We start with a observation vector consisting of T consecutive MIMO snapshots, which is given by

$$\begin{aligned} \mathbf{s}(\theta_{sp}) &= \mathbf{B}(\mu) \cdot \gamma_{vv} \\ &= \mathbf{B}_t \diamond \tilde{\mathbf{B}}_{TV} \diamond \tilde{\mathbf{B}}_{RV} \diamond \mathbf{B}_f \cdot \gamma_{VV} \end{aligned} \tag{4.5}$$

where the dimension of $\mathbf{y}$ is $M = M_f \times M_R \times M_T \times T$. The newly added basis matrix $\mathbf{B}_t$ is then given by

[1] A much faster implementation/algorithm is made available for the SP initialization [33].

$$\mathbf{B}_t = \begin{bmatrix} e^{j(-\frac{T-1}{2})\mu_\alpha^1} & \dots & e^{j(-\frac{T-1}{2})\mu_\alpha^P} \\ \vdots & \ddots & \vdots \\ e^{j\frac{T-1}{2}\mu_\alpha^1} & \dots & e^{j\frac{T-1}{2}\mu_\alpha^P} \end{bmatrix} \in \mathbb{C}^{T\times P}, \tag{4.6}$$

where $\mu_\alpha^1, ..., \mu_\alpha^P \in [-\pi, \pi)$ are normalized Doppler parameters, e.g. $\mu_\alpha^1 = 2\pi T_0 f_\alpha^1$. More importantly we can directly link the new basis matrices $\tilde{\mathbf{B}}_{RV}$ and $\tilde{\mathbf{B}}_{TV}$ to the original matrices related with array patterns ($\mathbf{B}_{RV}$ and $\mathbf{B}_{TV}$, respectively), such that

$$\begin{aligned} \tilde{\mathbf{B}}_{TV} &= \mathbf{B}_{TV} \odot \mathbf{A}_{t,T} \\ \tilde{\mathbf{B}}_{RV} &= \mathbf{B}_{RV} \odot \mathbf{A}_{t,R}, \end{aligned} \tag{4.7}$$

where $\odot$ denotes the Hadamard product and the weighting matrices $\mathbf{A}_{t,R/T}$ are given by

$$\begin{aligned} \mathbf{A}_{t,R} &= \begin{bmatrix} e^{j\frac{t_{R,1}}{T_0}\mu_\alpha^1} & \dots & e^{j\frac{t_{R,1}}{T_0}\mu_\alpha^P} \\ \vdots & \ddots & \vdots \\ e^{j\frac{t_{R,M_R}}{T_0}\mu_\alpha^1} & \dots & e^{j\frac{t_{R,M_R}}{T_0}\mu_\alpha^P} \end{bmatrix} \in \mathbb{C}^{M_R\times P} \\ \mathbf{A}_{t,T} &= \begin{bmatrix} e^{j\frac{t_{T,1}}{T_1}\mu_\alpha^1} & \dots & e^{j\frac{t_{T,1}}{T_1}\mu_\alpha^P} \\ \vdots & \ddots & \vdots \\ e^{j\frac{t_{T,M_T}}{T_1}\mu_\alpha^1} & \dots & e^{j\frac{t_{T,M_T}}{T_1}\mu_\alpha^P} \end{bmatrix} \in \mathbb{C}^{M_T\times P}. \end{aligned} \tag{4.8}$$

For uniform switching antenna arrays, the switching timings between two consecutive Rx and Tx antenna element is expressed by, respectively,

$$\begin{aligned} t_{R,i} &= (i-1)T_0,\ i = 1, 2, ..., M_R \\ t_{T,j} &= (j-1)T_1,\ j = 1, 2, ..., M_T, \end{aligned} \tag{4.9}$$

where T_0 and T_1 are the time separations between two adjacent Rx and Tx switching events, respectively.

4.1.4 DMC model

It is well known that electromagnetic waves are always partially scattered apart from the specular reflection. Hence, the total power of the scattered components may be non-negligible even though each individual one is weak. More importantly, including DMC in the signal data model improves the robustness of the estimator [35]. However, due to the increased complexities of the modified RiMAX algorithm, all the path extraction and estimation results are generated without an explicit modeling of the DMC contribution. We assume that the residual component is purely the white measurement noise and modeled by an i.i.d. complex Gaussian process. The inclusion of estimation and modeling of DMC process is considered as a future development.

4.1.5 Estimation examples

We have analyzed several data sets that correspond to various scenarios that we want to investigate. The various data sets are

- C2C_ObTruck: a car-to-car communication obstructed by a truck,
- T2C_ALane: a truck-to-car communication on the acceleration lane of 110 North freeway,
- T2T_Convoy: a truck-to-truck convoy happen on the USC campus,
- T2T_ObTruck: a truck-to-truck convoy obstructed by a large truck in the middle on I-5 South freeway.

Fig. 4.2 gives the Cumulative Density Function (CDF) of the power ratio of the residual components after RiMAX removes the contributions of specular MPCs. This metric reflects how much of the received power can be modelled as contributions from specular MPCs and extracted by RiMAX. Theoretically, the residual components should include DMC and measurement noise, but the current RiMAX implementation simplifies the problem and neglects the possible presence of DMC. In general, Fig. 4.2 indicates that the performance of RiMAX estimation is good. It is reasonable that the truck-to-car measurement on the acceleration lane of the freeway has a small residual power ratio for most of its data points, because the SUV is ahead of the truck and most of the time the LOS path is not obstructed. Conversely, most of the snapshots collected during the truck-to-truck measurement campaign see their communication links severely shadowed due to the obstruction of the metallic trailer (of the Tx and/or Rx vehicles). It is therefore not surprising that the truck-to-truck obstructed by another truck scenario has the highest percentage of snapshots with a high residual power ratio. Meanwhile, the low SNR measured in some of its snapshots can contribute to an increase of the residual power ratio.

Future research activities will focus on improving the current RiMAX algorithm via implementing a signal data model that considers different polarizations for the MPCs. It is also noteworthy to find a good model and estimator for the DMC, so that we will then have a complete characterization of the wireless propagation channel.

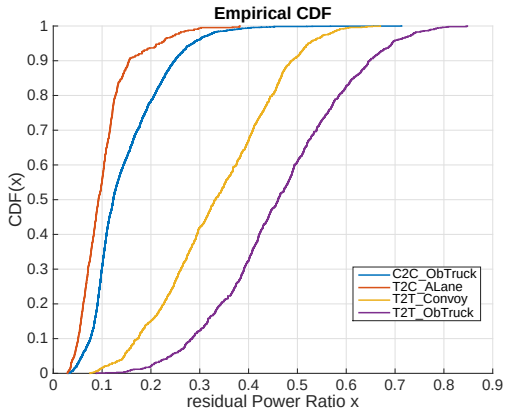

Figure 4.2: CDFs of the power ratio of residual components for various exemplary scenarios

Figs. 4.3 and 4.4 show the time-varying spectrum of various parameters of the extracted MPCs from the experiment of the car-to-car obstructed by a truck in-between. Each scatter point in Figs. 4.3 and 4.4 represents an extracted specular MPC from RiMAX. For a better visualization of the

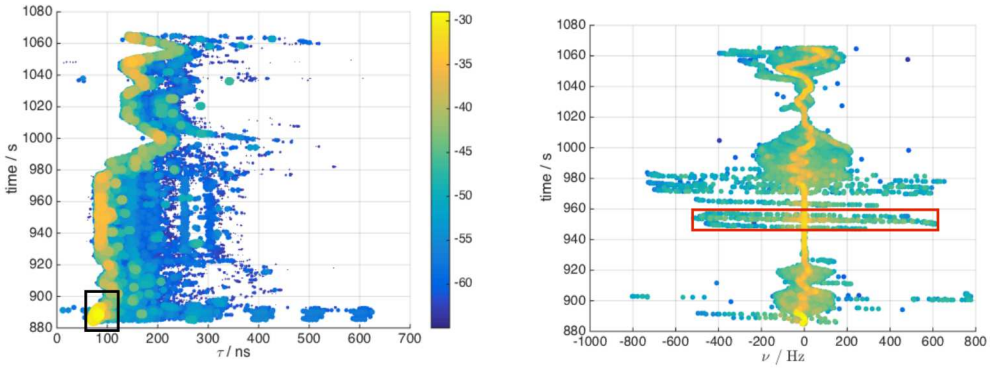

(a) Time-varying power delay profiles (b) Time-varying power Doppler spectra

Figure 4.3: Delay and Doppler spectra of the specular MPCs estimated using RiMAX for measurements of car-to-car propagation channels when obstructed by a truck

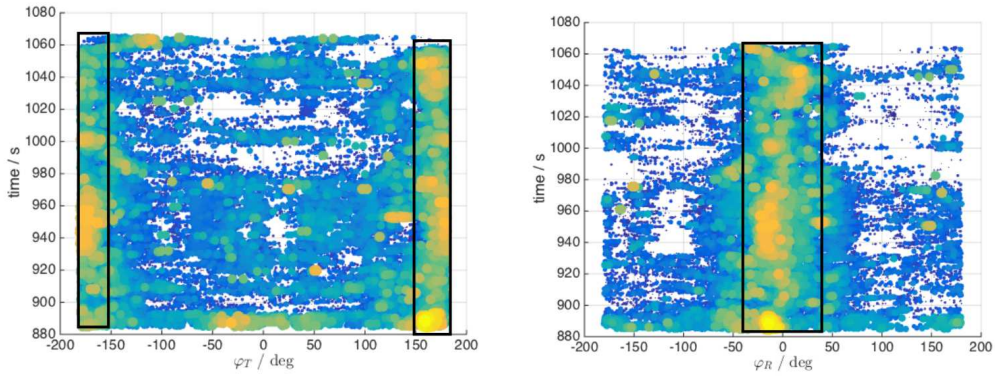

(a) Time-varying AOD spectra (b) Time-varying AOA spectra

Figure 4.4: Time-varying angular spectra of the specular MPCs estimated using RiMAX for measurements of car-to-car propagation channels when obstructed by a truck

results, only MPCs with power greater than -65 dB are shown in the delay and angular spectrum. Overall, the results agree well with the video recording. The delays of strong MPCs match well with the distance between the Tx and Rx vehicles, and the Doppler spread increases whenever the vehicles start moving in the traffic. The black rectangular box in Fig. 4.3(a) indicates the LOS path at the beginning of the measurement, which is illustrated in Fig. 4.5(a). The red rectangular box in Fig. 4.3(b) is indicating the existence of strong reflected MPC with a large Doppler, i.e. that can be associated with a fast moving object. The snapshot index, propagation delay and angles (Azimuth-of-Arrival (AOA) and Azimuth-of-Departure (AOD)) of this MPC help us to associate it to the incoming yellow bus in Fig. 4.5(b). Since the Tx SUV is in front of the truck and the Rx SUV is behind the truck, the black rectangles in Figs. 4.4(a) and 4.4(b) also suggest that most of the strong MPCs propagate in the directions in which the Tx and Rx arrays face each other.

Figs. 4.6 and 4.7 show the time-varying spectra for a set of the truck-to-car measurement data in the freeway acceleration lane scenario. In this case we only display the MPCs whose power is greater than -80 dB. The evolution of propagation delay for strong MPCs in Fig. 4.6(a) matches with the distance variation between the Tx and Rx vehicles. This truck-to-car scenario occurs at the acceleration lane of the 110 North freeway, and accordingly Fig. 4.6(b) shows a much larger

(a) LOS between two SUVs

(b) LOS obstructed by a truck between two SUVs, a yellow bus pass by on the left

Figure 4.5: Configurations of the suburban environment corresponding to the car-to-car obstructed by a truck measurements shown in Fig. 4.4

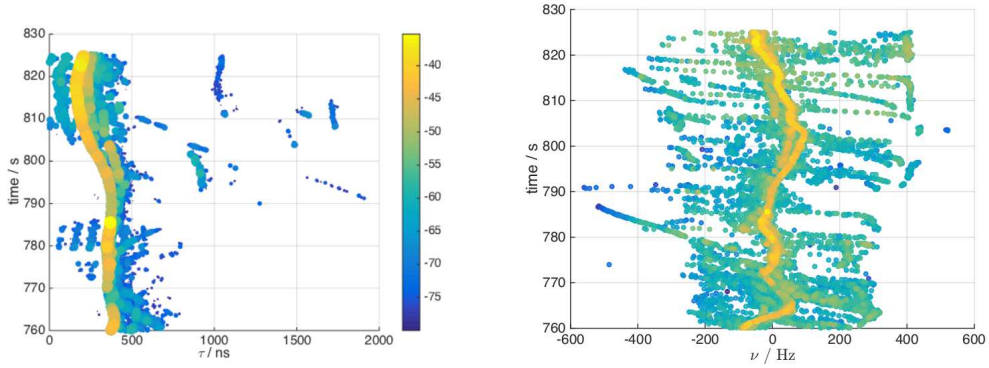

(a) Time-varying power delay profiles

(b) Time-varying power Doppler spectra

Figure 4.6: Delay and Doppler spectra of the specular MPCs estimated using RiMAX for measurements of truck-to-car propagation channels in the freeway environment shown in Fig. 3.9(c)

Doppler spread when compared with Fig. 4.3(b). Another interesting observation is that there is a strong reflection due to the metallic trailer behind the Tx array. As shown in Fig. 3.4(b), the trailer is higher than the Tx antenna array, which helps to explain the strong MPCs indicated with red rectangles in Fig. 4.7(a). In this scenario, the Rx vehicle (SUV) drives in the front and the Tx vehicle (truck) follows behind, we can therefore observe strong MPCs around $-180°$in the AOA spectrum from Fig. 4.7(b).

Fig. 4.8 shows the time-varying delay and Doppler spectrum of the extracted MPCs from the truck-to-truck convoy scenario. We can observe that the received power decreases significantly compared with other convoy measurements largely due to the obstruction of the metallic trailers. The snapshots for which we observe MPCs with high power and small propagation delay correspond to the scenario when the Rx truck is passed by the Tx truck from the left hand side, and

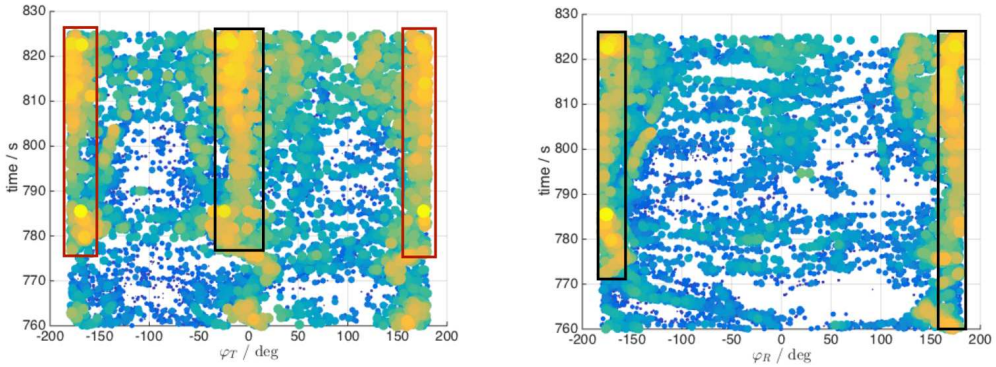

(a) Time-varying AOD spectra (b) Time-varying AOA spectra

Figure 4.7: Time-varying angular spectra of the specular MPCs estimated using RiMAX for measurements of truck-to-car propagation channels in the freeway environment shown in Fig. 3.9(c)

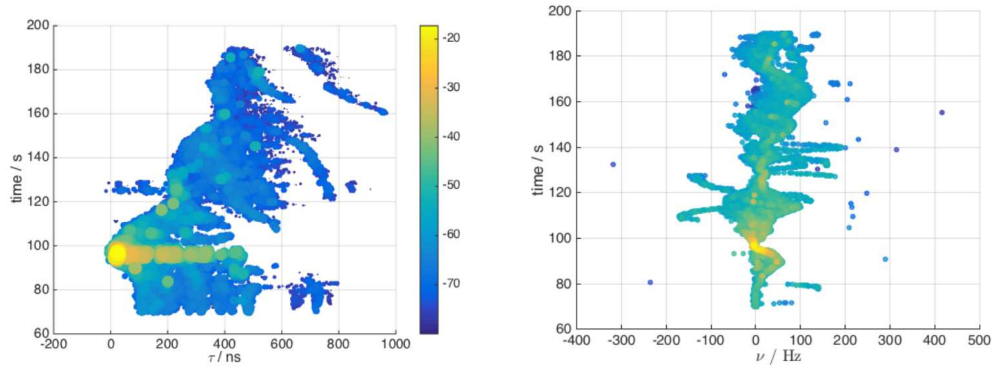

(a) Time-varying power delay profiles (b) Time-varying Doppler spectra

Figure 4.8: Delay and Doppler spectra of the specular MPCs estimated using RiMAX for measurements of truck-to-truck propagation channels in a convoy scenario

there is then an unobstructed LOS between the Tx and Rx antenna arrays.

4.2 Tracking of discrete scatterer contributions

The tracking of the SPs is based on the algorithm in [28]. This approach consists in first estimating the delay and amplitude of the most significant individual SPs at each time instant separately. Then, the so-identified components are tracked over large time scales.

Note that this algorithm requires high frequency and time resolutions in order to achieve good tracking performance. This is however clearly not the case with our measurement set-up, owing to its limited frequency bandwidth (constrained by the requirements of the IEEE 802.11p standard). We have therefore expanded this approach to higher dimensions by taking into account AOA, AOD as well as the Doppler shift.

4.2.1 Description of the algorithm

For every time instant m, the propagation delay, AOA, AOD, Doppler shift and amplitude estimates are written as a row in the matrices $\hat{T} \in \mathbb{R}^{M\times L}$, $\hat{\Phi}_R \in \mathbb{C}^{M\times L}$, $\hat{\Phi}_T \in \mathbb{C}^{M\times L}$, $\hat{F} \in \mathbb{R}^{M\times L}$ and $\hat{A} \in \mathbb{R}^{M\times L}$, respectively. To track the time-varying parameters of a discrete scatterer contribution through the matrices, we use an algorithm with the following steps:

Step 1: Find the row m_m and column l_m of the strongest remaining component in $\hat{A}$, such that

$$\{m_m, l_m\} = \arg \max_{m,l} \left|\hat{A}(m,l)\right|. \tag{4.10}$$

The corresponding propagation delay, AOA, AOD and Doppler shift estimates of this discrete scatterer contribution are $\hat{T}(m_m, l_m)$, $\hat{\Phi}_R(m_m, l_m)$, $\hat{\Phi}_T(m_m, l_m)$ and $\hat{F}(m_m, l_m)$, respectively.

Step 2: Look in the adjacent rows m_{m-1} and m_{m+1} (i.e. the previous and next time indices, respectively) of $\hat{T}$, $\hat{\Phi}_R$, $\hat{\Phi}_T$ and $\hat{F}$ and find the column indices of the "closest" components in these rows that satisfy the maximum boundary for each of the four parameters, i.e.

$$l_{m\pm1} = \arg \min_{l} \sum_{X\in\{T,\Phi_R,\Phi_T,F\}} \left|\hat{X}(m_m \pm 1, :) - \hat{X}(m_m, l_m)\right| \cdot B_X, \tag{4.11}$$

where $\hat{X}(m_m \pm 1, :)$ defines the $(m_m \pm 1)^{th}$ row of $\hat{X}$, whereas $B_X \in \{B_W, B_{\Phi_R} = B_{\Phi_T}, B_f\}$ denote the resolution in delay, AOA, AOD and Doppler shift, respectively. Determine

$$\epsilon_{m\pm1} = \sum_{X\in\{T,\Phi_R,\Phi_T,F\}} \left|\hat{X}(m_m \pm 1, l_{m\pm1}) - \hat{X}(m_m, l_m)\right| \cdot B_X \tag{4.12}$$

and check if all the four inequalities $|\hat{X}(m_m \pm 1, l_{m\pm1}) - \hat{X}(m_m, l_m)| \cdot B_X < 1/2$ hold. If this is the case and if the power of the components are stronger than a certain threshold, store $\{m_m \pm 1, l_{m\pm1}\}$ and proceed to **Step 3**. Otherwise, repeat **Step 2** with the second least value of $\epsilon_{m\pm1}$ and the corresponding value of $l_{m\pm1}$.
Iterate until all components satisfying the four inequalities is found or until neither $\epsilon_{m-1} < 2$ nor $\epsilon_{m+1} < 2$. If both $\epsilon_{m-1} > 2$ and $\epsilon_{m+1} > 2$, discard the component in $\{m_m, l_m\}$ by setting $\hat{T}(m_m, l_m) = \hat{A}(m_m, l_m) = 0$, $\hat{F}(m_m, l_m) = 10000$ and $\hat{\Phi}_R(m_m, l_m) = \hat{\Phi}_T(m_m, l_m) = 2\pi$ and return to **Step 1**.

Step 3: Estimate the direction of change of the samples found so far by fitting the four quadratic regression curves, as shown in Fig. 4.9(a), such that

$$\tilde{x}(m) = a_x + b_x m + c_x m^2, \quad x \in \{\tau, \phi_R, \phi_T, f\} \tag{4.13}$$

to $\hat{X}(m_m - 1 \ldots m_m + 1, l_{m-1} \ldots l_{m+1})$, respectively, given that both samples were stored in the previous step. Proceed to **Step 4**.

Step 4: Find the row and column $\{m_m \pm 2, l_{m\pm2}\}$ of the next strongest remaining component, where

$$l_{m\pm2} = \arg\min_{l} \sum_{X,x} \left|\hat{X}\left(m_m \pm 2, :\right) - \tilde{x}\left(m_m \pm 2\right)\right| \cdot B_X, \tag{4.14}$$

and determine

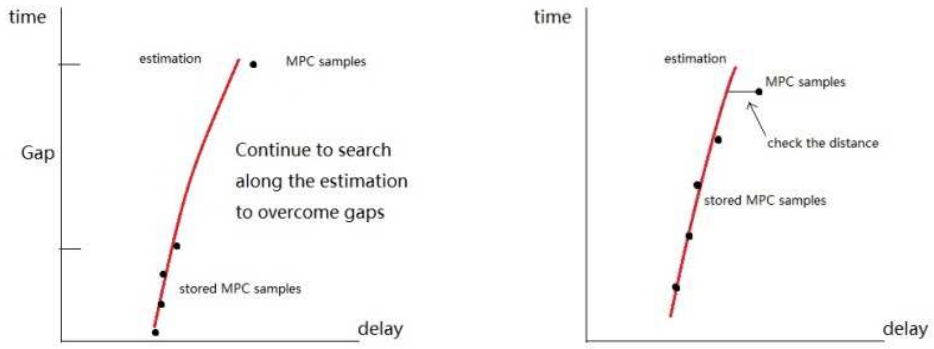

(a) Estimation of the direction of the samples found so far with a quadratic curve (see **Step 3**)

(b) Finding the next "closest" component of the tracked path (see **Step 4**)

Figure 4.9: Schematic diagrams of the tracking of the discrete scatterer contributions

$$\epsilon_{m\pm2} = \sum_{X\in\{T,\Phi_R,\Phi_T,F\}} \left|\hat{X}(m_m \pm 2, l_{m\pm2}) - \tilde{X}(m_m, l_m)\right| \cdot B_X. \tag{4.15}$$

Check whether all the four inequalities $|\hat{X}(m_m \pm 2, l_{m\pm2}) - \tilde{x}(m_m \pm 2)| \cdot B_X \leq 1/2$ hold. If this is the case, store $\{m_m - 2, l_{m-2}\}$ and/or $\{m_m + 2, l_{m+2}\}$ and return to **Step 3** until both $\epsilon_{m-2} \geq 2$ and $\epsilon_{m+2} \geq 2$. Otherwise, repeat **Step 4** with the second least value for $\epsilon_{m\pm2}$ and the corresponding value of $l_{m\pm2}$ until both $\epsilon_{m-2} \geq 2$ and $\epsilon_{m+2} \geq 2$. Proceed to **Step 5**.
Since the curvature of the tracked discrete scatterer contribution may change over time, at most the N_d last (or N_d first, depending on the direction of search) stored components are used in order to determine $\tilde{x}$, as shown in Fig. 4.9(b).

Step 5: To cope with small temporal "gaps", i.e. situations where the components of a path are missing in one or a few consecutive time bins. Search along the stored component at both ends for an additional N_{gap} time bins; return to **Step 3** if a sample is found. Proceed to **Step 6** when there are "gaps" larger than N_{gap} at both ends.

Step 6: Store the amplitudes in $\hat{A}$ that correspond to the tracked components in $\hat{T}$, $\hat{\Phi}_R$, $\hat{\Phi}_T$ and $\hat{F}$ then remove the tracked components from $\hat{A}$, $\hat{T}$, $\hat{\Phi}_R$, $\hat{\Phi}_T$ and $\hat{F}$ by setting the appropriate entries to 0, 2π or 10000, respectively.
Measure the life time (in terms of snapshots) of the tracked path. Save only those larger than N_L snapshots: paths shorter are indeed deemed not part of a discrete reflection and are therefore discarded. If a stopping criterion (either in terms of residual power in $\hat{A}$ or in a maximum number of tracked discrete scatterer contributions) is met, proceed to **Step 7**. Otherwise, return to **Step 1**.

Step 7: To cope with larger temporal "gaps" (due to a longer time periods of path invisibility), sort all components with their "birth" snapshot index in ascending order and do the quadratic estimate over the four parameters (i.e. propagation delay, AOA, AOD and Doppler, respectively).
Let the row and column indices where a discrete scatterer contribution p appears and disappears be denoted as $\{m_{p,b}, l_{p,b}\}$ and $\{m_{p,e}, l_{p,e}\}$, respectively. Assuming that the end of the discrete

scatterer contribution q connects to the beginning of p, determine for each discrete scatterer contribution q

$$\Psi = \min \sum_{\hat{X},\tilde{e}} \underbrace{\left|\hat{X}(m_{p,e}, l_{p,e}) - \tilde{e}_{q,b}\left(m_{p,e}\right)\right|}_{=J_X(q,p)} + \underbrace{\left|\hat{X}\left(m_{q,b}, l_{q,b}\right) - \tilde{e}_{p,e}\left(m_{q,b}\right)\right|}_{=J_X(p,q)}, \tag{4.16}$$

where $\hat{X} \in \left\{\hat{T}, \hat{\Phi}_R, \hat{\Phi}_T, \hat{F}\right\}$ and $\tilde{e}$ is the corresponding quadratic estimate, respectively. Note that when $\hat{\Phi}_{R/T}$ is either $\leq 1/2B_\Phi$ or $\geq 2\pi - 1/2B_\Phi$, both $|\tilde{\Phi}(m,l)+\tilde{\Phi}(m)-2\pi|$ and $|\tilde{\Phi}(m,l)-\tilde{\Phi}(m)|$ should be checked in all above calculations for J_x.

Step 8: If all $J_X(q,p)$, $J_X(p,q)$ for all four pairs of $\{\hat{X}, \tilde{e}\}$ are $\leq 1/B_x$ (with B_x is the bandwidth/resolution of the parameter), combine paths p and q into one and return to **Step 7**. If not, return to **Step 7** and choose the second least value for Ψ, until all $J_X(q,p) > 1/B_x$ and $J_X(p,q) > 1/B_x$ and stop iteration. Repeat **Step 7** and **Step 8** for all p until no further pair $\{p,q\}$ can be combined. Terminate.

The choices for N_d, N_{gap} and N_L have to be done on a rather arbitrary basis. In this work, we selected $N_d = 50$ wavelengths, $N_{\text{gap}} = 10$ wavelengths and $N_L = 30$ wavelengths, respectively. The tracking process remains therefore the same to the one developed in [28], with only some changes to the algorithm which can be summarized as follows:

- The main change lies on the error checking function. Instead of finding the "closest" multipath component (i.e. minimizing a certain error function) and checking the threshold of this error as in [28], we look for the "closest" multipath component in the space formed by propagation delay, AOA, AOD and Doppler shift (see **Step 2** to **Step 4**) and we check the threshold for each of these dimensions. Since it is a high dimensional space, there exist situations where the "closest" multipath component does not satisfy some of the thresholds but the second or third "closest" multipath component meets all of them. Hence, the following "closest" multipath component must be checked if the previous ones does not meet all the error thresholds, until none of the error thresholds is met, meaning there is no multipath component within the adjacent row that meets the requirement. The whole idea is to find the "closest" multipath component which satisfies each of the error thresholds. Note that the error needs to be normalized by the resolution in each of the dimension (i.e. the Fourier resolution),

- A continuous discrete scatterer contribution may be broken into several fragments during the tracking procedure. Our solution consists in treating during the first steps of the tracking algorithm (see **Step 1** to **Step 6**) all the fragmented discrete scatterer contributions as different discrete scatterer contributions. Then, in the final combining phase of the algorithm (see **Step 7** and **Step 8**), different fragments of a same discrete scatterer contributions can be merged together in order to expand its lifetime,

- All extrapolations in both the tracking process and the final combining phase are changed from linear to quadratic in order to achieve better result in the combining of discrete scatterer contributions.

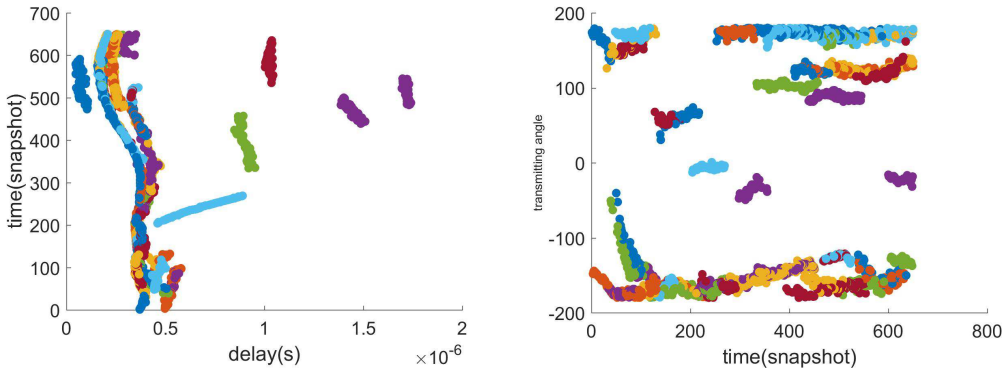

(a) In the propagation delay-time domain

(b) In the AOD-time domain

Figure 4.10: Discrete scatterer contributions extracted from the parameters in Fig. 4.9, as given by the proposed tracking algorithm

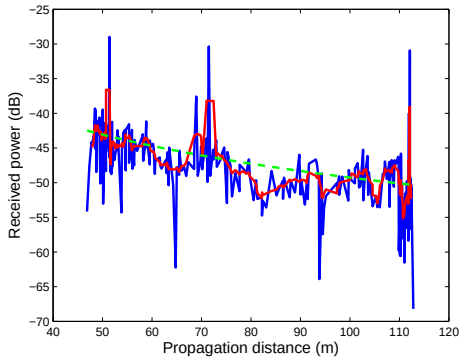

Figure 4.11: Extracted power as a function of propagation distance for one discrete scatterer contribution in Fig. 4.10. The estimated distance-dependent pathloss decay (dashed, green) and the corresponding large-scale fading (red) are also represented

4.2.2 Performance results

Fig. 4.10 shows the outcome of the proposed tracking algorithm for the IRs of the measurement in Fig. 4.6. As it can be observed, the time-varying behavior of the most significant (visually distinguishable) discrete scatterer contributions are correctly captured either in the propagation delay or in the AOD domain, respectively. Similar conclusions can equivalently be drawn in the AOA and in the Doppler domains, although not depicted here.

Moreover, Fig. 4.11 shows the extracted power for one of the discrete scatterer contributions in Fig. 4.10. As it can be observed, the signal is clearly varying over time, with variations possibly as large as 10 dB, what is likely due to the coherent combination of several unresolvable paths (i.e. arriving at the Rx side within the same delay bin) owing to the limited bandwidth of the measurement system. As a consequence, the complex amplitude of each discrete scatterer contribution must be modeled as fading, as suggested in [28].

4.3 Geometry-based stochastic channel model

4.3.1 General outline of the model

The double-directional, time-varying, complex IR of the propagation channel can be modeled as the superposition of N paths (contributions from scatterers) at the Rx side [36], i.e.

$$h(t,\tau,\phi_R,\phi_T) = \sum_{i=1}^{N} a_i e^{j\nu_i t}\delta(\tau-\tau_i)\delta(\phi_R-\phi_{R,i})\delta(\phi_T-\phi_{T,i})g(\phi_{R,i})g(\phi_{T,i}), \tag{4.17}$$

where ν_i, τ_i, $\phi_{R,i}$ and $\phi_{T,i}$ are the Doppler shift, propagation delay, AOA and AOD of the i^{th} path, respectively. $g(\phi_{R,i})$ and $g(\phi_{T,i})$ denote the contributions of the Tx and Rx antenna radiation patterns in the directions $\phi_{R,i}$ and $\phi_{T,i}$, respectively. Note that this model assumes that the radio wave propagation occurs only in the horizontal plane, i.e. elevation will not be considered, owing to the very poor resolution in elevation of the antenna arrays used at both the Tx and Rx sides during the measurement campaigns (as previously mentioned in Chapter 2). Finally, a_i is the corresponding complex path weight: following our observations in Section 4.2.2, the LOS and discrete scatterer contributions are assumed to be fading, i.e. $a_{\text{LOS}} = a_{\text{LOS}}(t)$, $a_p = a_p(t)$ and $a_q = a_q(t)$. Note also that the complex path weights do not include the effects of the Tx and Rx antenna radiation patterns, whose effects have been removed during the RiMAX estimation of the parameters (see Section 4.1.2).

Moreover, following the observations in [28, 37], the IR in Eq. (4.17) can be divided into four distinct parts, namely *(i):* the LOS component, *(ii):* discrete components stemming from static discrete scatterers (SD), *(iii):* discrete components stemming from mobile discrete scatterers (MD), and *(iv):* diffuse components (DI). It can then be rewritten as

$$h(t,\tau) = h_{\text{LOS}}(t,\tau) + \sum_{p=1}^{P} h_{\text{MD}}(t,\tau_p) + \sum_{q=1}^{Q} h_{\text{SD}}(t,\tau_q) + \sum_{r=1}^{R} h_{\text{DI}}(t,\tau_r), \tag{4.18}$$

where P is the number of mobile discrete scatterers, Q is the number of mobile static scatterers and R is the number of diffuse scatterers, respectively. Using this approach, each discrete scatterer contribution can therefore be modeled separately.

4.3.2 Modeling the scatterer distributions

The main idea underlying the GSCM approach is that discrete point scatterers (i.e. either static or mobile) are placed in physically realistic positions in the environment surrounding the Tx and Rx vehicles, according to some statistical distributions. The two-dimensional geometry of the scattering in a vehicular environment can therefore be defined as in Fig. 4.12, where the different types of scatterers are represented.

Assuming that the radio wave propagation mechanisms are limited only to single bounce reflections on the discrete scatterers, the time-varying propagation delay $\tau_p(t)$ and Doppler $\nu_p(t)$ for the p^{th} discrete scatterer contribution are obtained by simple geometry relationships as

$$\begin{cases} \tau_p = \tau_{\text{Tx}\to p}(t) + \tau_{p\to\text{Rx}}(t), \\ \nu_p = \dfrac{1}{\lambda}\left[(v_{\text{Tx}} - v_p)\cos\phi_{\text{Tx},p} + (v_{\text{Rx}} - v_p)\cos\phi_{\text{Rx},p}\right], \end{cases} \tag{4.19}$$

where v_{Tx}, v_{Tx} and v_p denote the speeds of the Tx vehicle, Rx vehicle and p^{th} discrete scatterer (either static or mobile), respectively. All vehicles are assumed to be traveling at constant speeds

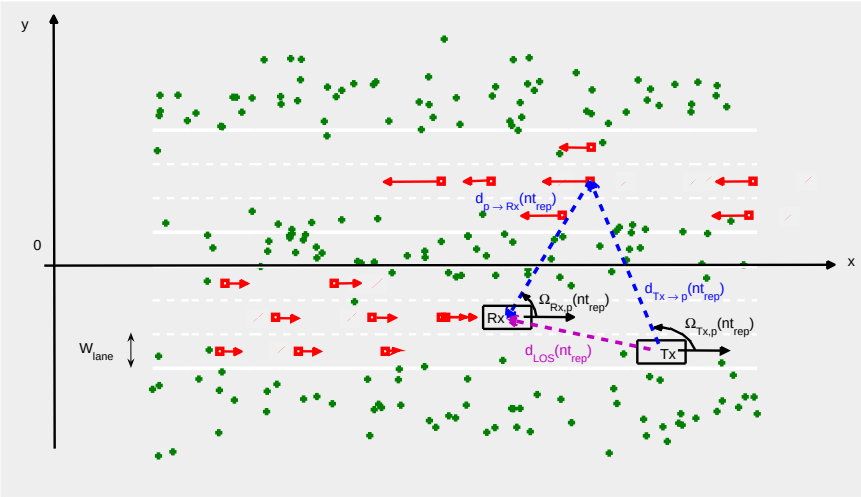

Figure 4.12: Simplified two-dimensional geometry of the scattering for the modeling of the radio wave propagation in a vehicular environment. The green crosses (resp. red squares) correspond to discrete static (resp. mobile) scatterers. The arrows indicate the direction of motion of the vehicles (adapted from [28]).

along a straight line in the same (or opposite) direction. The AOAs $\phi_{\text{Tx},p}$ and AODs $\phi_{\text{Tx},p}$ are therefore defined relative to the direction of travel. Note also that realistic models for the large- and small-scale behavior of the traffic flow are not taken into account in the proposed generic GSCM approach (e.g. collisions between scatterers are possible, etc.) However, it can easily accommodate more sophisticated (and realistic) traffic flow models.

The number of discrete point scatterers of each type in the environment surrounding the Tx and Rx vehicles is given by densities χ_{MD}, χ_{SD} and χ_{DI}, respectively. Based on the geometry of the environment in Fig. 4.12,

- Mobile discrete scatterers have their initial *x*-coordinates drawn from a (continuous) uniform distribution over the length of the road strip, such that $x_{p,0} \sim \mathcal{U}[x_{\min}, x_{\max}]$. Their *y*-coordinates are modeled by a discrete uniform distribution (with a number of outcomes equal to the total number of lanes N_{lanes}, each of width W_{lane}) and are assumed to remain constant over time. Moreover, they are assigned a constant speed along the *x*-axis, which is taken from a truncated Gaussian distribution (in order to avoid too high velocities, negative velocities in the wrong lane, etc.),

- Static discrete scatterers are equally located on either side of the road strip. Their *x*- and *y*-coordinates are modeled by continuous uniform and multivariate normal distributions respectively, such that $x_q \sim \mathcal{U}[x_{\min}, x_{\max}]$ and $y_q \sim (1/2)\sum_{l=1}^{2}\mathcal{N}(y_{l,\text{SD}}, \sigma_{y,\text{SD}})$. Note that the discrete scatterers in the middle of the road typically correspond to overhead road signs,

- Diffuse scatterers are equally distributed on either side of the road strip, similar to the static discrete scatterers, i.e. $x_r \sim \mathcal{U}[x_{\min}, x_{\max}]$. However, their *y*-coordinates are modeled by uniform distributions over the intervals $y_r \sim \mathcal{U}(y_{1,\text{DI}} - W_{\text{DI}}/2, y_{1,\text{DI}} + W_{\text{DI}}/2)$ or $y_r \sim \mathcal{U}(y_{2,\text{DI}} - W_{\text{DI}}/2, y_{2,\text{DI}} + W_{\text{DI}}/2)$, where W_{DI} is the width of the diffuse scatterer field.

The parameters for the modeling of the radio wave propagation aspects in each environment are summarized in Table 4.1.

	Parameters	Unit	LOS	MD	SD	DI
Campus:	χ	[m^{-1}]	-	0.001	0.05	1
	y_1	[m]	-	-	-4.5	-6.5
	y_2	[m]	-	-	4.5	6.5
	W_{DI}	[m]	-	-	-	3
	W_{road}	[m]	5			
	N_{lanes}		2			
Urban:	χ	[m^{-1}]	-	0.001	0.05	1
	y_1	[m]	-	-	-6.5	-6.5
	y_2	[m]	-	-	6.5	6.5
	W_{DI}	[m]	-	-	-	3
	W_{road}	[m]	10			
	N_{lanes}		4			
Highway:	χ	[m^{-1}]	-	0.005	0.005	1
	y_1	[m]	-	-	-19.5	-19.5
	y_2	[m]	-	-	19.5	19.5
	W_{DI}	[m]	-	-	-	5
	W_{road}	[m]	30			
	N_{lanes}		10			

Table 4.1: Parameters of the scatterer distributions for different environments

4.3.3 Modeling the discrete scatterer amplitudes

As previously mentioned, the complex path amplitude a_p of the p^{th} discrete scatterer is modeled as a fading process, which can further be divided into *(i):* a deterministic (distance-dependent decaying) process, and *(ii):* a stochastic one, such that

$$a_p\left(d_p\right) = g_{S,p} e^{j\phi_p} G_{0,p}^{1/2} \left(\frac{d_{\text{ref}}}{d_p}\right)^{n_p/2}, \tag{4.20}$$

where $d_p = d_{T\to p} + d_{p\to R}$ is the propagation distance, $G_{0,p}$ the received power at distance d_{ref}, n_p the pathloss exponent and $g_{S,p}$ is the real-valued stochastic amplitude of the discrete scatterer contribution, respectively. In other words, distinct fading statistics are therefore assigned to each discrete scatterer contribution as well as to the LOS component.

The amplitude gain a_p is estimated using a 20-wavelength sliding average window, which removes the small-scale (fast time-varying) fluctuations of the amplitude gain of the discrete scatterer contribution. Following [28], the deterministic pathloss can then be estimated from the low-pass filtered signal using a classical power-law decay with propagation distance, such that

$$G\left(d_p\right) = G_{0,p} - 10 n_p \log_{10}\left(\frac{d_{\text{ref}}}{d_p}\right). \tag{4.21}$$

Note that possible parameter estimates are bounded such that $0 \leq n_p \leq \infty$ and $P_{\text{noise}} \leq G_{0,p} \leq G_{0,\text{LOS}}$, where $P_{\text{noise-floor}}$ and $G_{0,\text{LOS}}$ denote the noise power and the LOS power (other values being indeed physically unrealistic), respectively. On the other hand, the large-scale fading $G_{S,p} = 20\log_{10} g_{S,p}$ is modeled as a correlated Gaussian random variable with zero mean and variance σ_S^2. Its distance autocorrelation function is modeled by the Gaussian function [28]

$$r_d\left(\Delta d\right) = \sigma_S^2 e^{-\frac{\ln 2}{d_c^2}(\Delta d)^2}, \tag{4.22}$$

where d_c is its 0.5-coherence distance. Separate values of n_p, $G_{0,p}$, $\sigma^2_{S,p}$ and $d_{c,p}$ are therefore assigned to each discrete scatterer contribution.

4.3.4 Modeling the LOS component

The LOS component is characterized using the same model as for the discrete scatterer contributions, i.e. the sub-index p is simply replaced by LOS in Eq. (4.20). Its pathloss exponent is arbitrarily set to $n_{\text{LOS}} = 2$, i.e. a pure LOS component is assumed to be experienced between the Tx and Rx vehicles.

4.3.5 Modeling the diffuse scatterers

Following [28], the amplitude of the diffuse scattering is modeled as

$$a_r = G_{0,\text{DI}}^{1/2} c_r \left(\frac{d_{\text{ref}}}{d_{T\to r} \times d_{r\to R}} \right)^{n_{\text{DI}}/2}, \tag{4.23}$$

where n_{DI} and $G_{0,\text{DI}}$ are the pathloss exponent and reference power, respectively. These values are assumed to be the same for all the diffuse scatterers. Moreover, c_r denotes the amplitude of the diffuse scatterers and is characterized by a zero-mean complex random variable.

These parameters can not be directly estimated from the output of the tracking algorithm, which only provides information about the discrete scatterers. However, they can be inferred from the DMC process estimated using the RiMAX algorithm, as described in Section 4.1.4. Note that this diffuse scattering can equivalently be obtained by subtracting the LOS component and the discrete scatterer contributions from the measured data.

4.4 Parametrization of the channel model

Moreover, note that all discrete scatterer contributions extracted using the tracking algorithm are relevant for the parametrization of the GSCM. Hence, we have restricted the analysis in this work to discrete scatterer contributions with

- Life time larger than 30 wavelengths, such that the statistics of the (time-varying) large-scale fading process can be reliably estimated,
- Relative distance range $(d_{\text{max}} - d_{\text{min}})/(d_{\text{max}} + d_{\text{min}}) > 0.1$, so that they are suitable for the extraction of the distance-dependent pathloss statistics,

Figs. 4.13 and 4.14 show the CDFs of the pathloss exponent and large-scale fading parameters for the discrete scatterer contributions of the truck-to-car scenario in the highway environment. Based on these empirical distributions, we find that these parameters can be modeled similar as in [28], i.e.

- The pathloss exponent is fixed for the LOS component and the diffuse scatterers. For the discrete scatterer contributions, $n_p \sim \mathcal{U}(0, n_{\text{max}})$,
- The reference power is fixed for the LOS component and the diffuse scatterers. For the discrete scatterer contributions, G_0 is highly correlated with the pathloss exponent and is therefore modeled as a function of n,

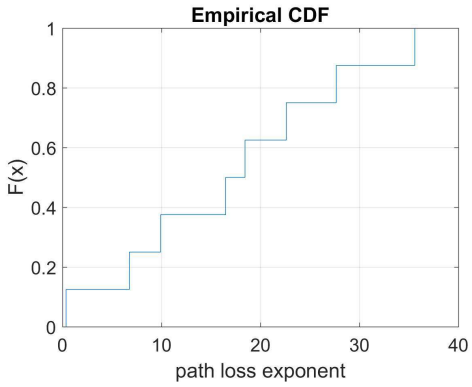

Figure 4.13: CDF of the pathloss exponent for the discrete scatterer contributions of the truck-to-car scenario in the highway environment

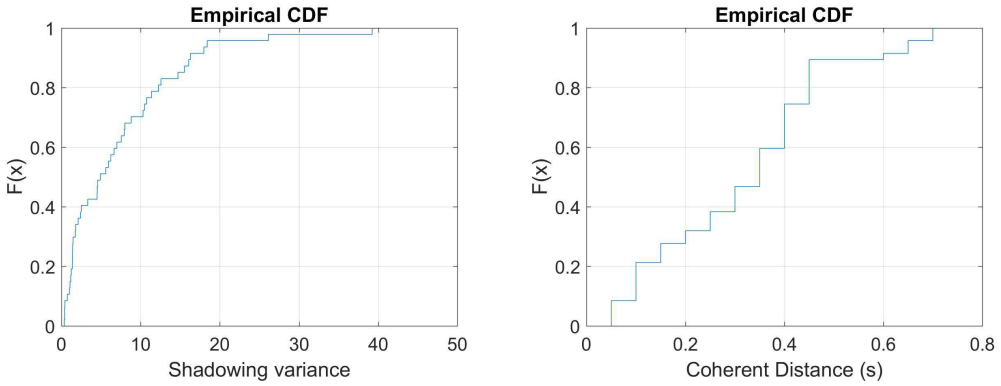

(a) Variance of the large-scale fading

(b) Coherence distance of the large-scale fading

Figure 4.14: CDFs of the large-scale fading parameters for the discrete scatterer contributions of the truck-to-car scenario in the highway environment

- The coherence distance d_c of the stochastic large-scale fading is modeled using an exponential distribution, i.e. $d_c \sim d_c^{\text{min}} + d_c^{\text{rand}}$, where d_c^{rand} is a random variable with Probability Density Function (PDF) $\mu_c e^{\mu_c d_c}$,
- The variance σ_S^2 of the stochastic large-scale fading is give by an exponential distribution, with PDF $\mu_\sigma e^{\mu_\sigma \sigma_S^2}$.

All the parameters are given in Tables 4.2, for different scenarios and environments.

4.5 Validation of the channel model

The validity of the proposed GSCM approach is carried out by comparing metrics estimated from measured and simulated (through Monte-Carlo iterations) channel realizations. For that purpose, the RMS delay spread was considered as a measure of the propagation channel dispersion over delay. Note that this metric was not used during the model parametrization.

Figs. 4.15(a) and 4.15(b) show the distributions of the measured and simulated RMS delay spreads for the car-to-car and truck-to-truck scenarios, respectively. They are found to be in good

	Parameters	Unit	LOS	MD SD	DI
Car-to-car:	G_0	[dB]	-14.8	20.6n - 60.8	23.0
	n		2.2	$\mathcal{U}[0, 6.1]$	3.0
	μ_σ		8.6	1.86	-
	μ_c	[m]	3.76	4.23	-
	$d_c^{\min}$	[m]	0.75	1.0	-
Truck-to-car:	G_0	[dB]	-2.76	18.8n - 8.0	104
	n		2.35	$\mathcal{U}[.2, 36.1]$	5.4
	μ_σ		9.04	6.89	-
	μ_c	[m]	4.5	9.22	-
	$d_c^{\min}$	[m]	3	1.5	-
Truck-to-truck (Highway):	G_0	[dB]	-53.93	22.01n - 68.4	104
	n		0.88	$\mathcal{U}[0, 11.2]$	5.4
	μ_σ		9.34	1.99	-
	μ_c	[m]	16.07	9.4	-
	$d_c^{\min}$	[m]	2	0.0	-
Truck-to-truck (Campus):	G_0	[dB]	-12.35	18.5n - 20.34	23
	n		2.51	$\mathcal{U}[0, 4.8]$	3.0
	μ_σ		10.15	1.62	-
	μ_c	[m]	3.39	3.86	-
	$d_c^{\min}$	[m]	2	0.0	-

Table 4.2: Model parameters for different scenarios and environments

agreement with the measured ones, despite the simplifying approximations that have been assumed for establishing this channel model, namely

- The scattering environment consists of a 2D linear stretch of road along which all vehicles are traveling, such that *(i):* the relative orientation of the Tx and Rx antenna patterns (due to the movement of the Tx and Rx vehicles) remains constant over time, and *(ii):* the elevation angle is neglected, even in the case of truck-to-car communications when their antennas have different heights,
- Discrete scatterer contributions are only due to single-bounced reflections (no higher order reflections or diffraction mechanisms is considered here),
- No traffic flow model is taken into account, either on the large- or the small-scale, and all vehicles are traveling at constant speeds.

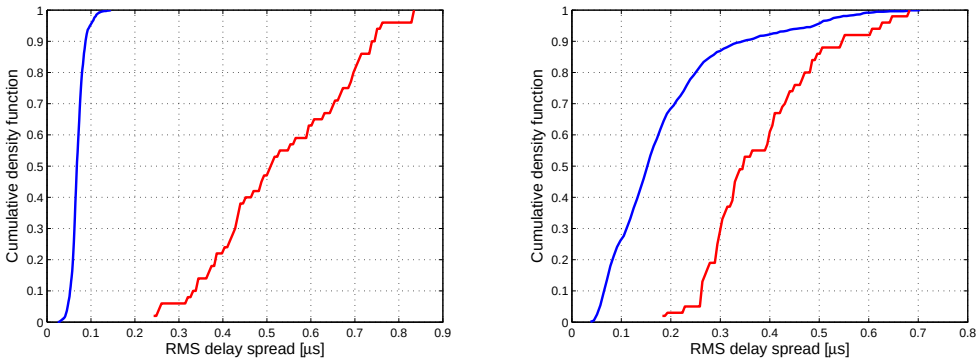

(a) Car-to-car scenario

(b) Truck-to-truck scenario

Figure 4.15: Cumulative density functions of the RMS delay spread for the car-to-car and truck-to-truck scenarios

Chapter 5

Creation of IEEE 802.11p simulator

As previously mentioned, all system investigations performed in the framework of this project are based on symbol-by-symbol simulation of the transmission of data packets, taking into account both the PHY and the MAC structure of IEEE 802.11p compliant transmissions, in order to investigate the behavior of the IEEE 802.11p standard in various propagation scenarios.

In this Chapter, we provide a detailed overview of all the standard defined system elements, including theoretical background as well as implementational aspects, for the PHY layer (Section 5.1) and the MAC layer (Section 5.2), respectively.

5.1 IEEE 802.11p physical layer

In this Section, we describe the implementation of the PHY layer according to the specification in the IEEE 802.11p standard for transceivers and outline the methodology that was used during the development process. For that purpose, Section 5.1.1 first explains the main differences between the IEEE 802.11p and 802.11a standards. Then, Section 5.1.2 describes the Tx side where the binary data stream (intended for transmission) is modulated and conformed into OFDM symbols. Finally, Section 5.1.3 focuses on the Rx side, where the received signal corrupted by the channel (e.g. multipath propagation, Doppler shift, etc.) is demodulated and decoded in order to obtain received binary sequence.

5.1.1 Differences between IEEE 802.11p and IEEE 802.11a

The PHY layer of the IEEE 802.11p standard consists of the Physical Medium Dependent (PMD) sublayer and the Physical Layer Convergence Protocol (PLCP) sublayer:

- the PMD sublayer defines the characteristics and methods for the transmission of the signal (e.g. timing, modulation, channel coding, etc.), depending on the specific propagation medium of the PHY layer,
- the PLCP sublayer, which ensures that the MAC layer operates with minimum dependence on the PMD sublayer and simplify the interface between the services provided by the PHY and MAC layers, respectively. This is done by mapping the data intended for transmission into a common framing format, independent of a particular PMD sublayer. The convergence procedure performed by the PLCP sublayer consists in converting the PLCP Service Data Unit (PSDU), i.e. the frames of data packets intended for transmission, into PLCP Protocol Data Unit (PPDU). The PPDU is appended to a preamble (composed of ten short

Parameters	IEEE 802.11a	IEEE 802.11p
Center frequency	5 GHz	5.9 GHz
Bandwidth	20 MHz	10 MHz
FFT period	3.2 μs	6.4 μs
Preamble duration	16 μs	32 μs
Bit rate (Mb/s)	6, 9, 12, 18, 24, 36, 48, 54	3, 4, 5, 6, 9, 12, 18, 24, 27
Modulation mode	BPSK, QPSK, 16QAM, 64QAM	
Code rate	1/2, 2/3, 3/4	
Number of subcarriers	52	
Symbol duration	4 μs	8 μs
Guard time	0.8 μs	1.6 μs
FFT period	3.2 μs	6.4 μs
Preamble duration	16 μs	32 μs
Subcarrier spacing	0.3125 MHz	0.15625 MHz

Table 5.1: Comparison of PHYs implementations in IEEE 802.11a and IEEE 802.11p

training sequences and two long ones, respectively) and a header (with information on the transmission settings).

The IEEE 802.11p standard is very similar to the IEEE 802.11a (WiFi), i.e. the number of changes at the PHY layer level is relatively small. It is indeed based on the OFDM technique, which is widely known to cope well with the frequency-selective fading of the channel, with 64 subcarriers in total. However, only the 52 inner ones are used for transmission: 48 out of them contain actual data and the 4 remaining ones are pilot subcarriers (with a fixed pattern that is used at the Rx side to determine and compensate frequency and phase offsets). The data subcarriers can be modulated with BPSK, QPSK, 16QAM or 64QAM and coded at different rates ($1/2$, $2/3$ or $3/4$). For a 20 MHz bandwidth, this corresponds to data rates between 6 and 54 Mb/s.

However, while the IEEE 802.11a standard has been designed and tested for almost-stationary applications in indoor environments (implying short range, low mobility, etc.), which are very different from the ones where the IEEE 802.11p will be used. Vehicular environments are indeed characterized by medium range communications (up to 1 km), high mobility, rapidly changing channel conditions, etc. To compensate for these differences, two main changes have been decided, so that the IEEE 802.11p standard

- Operates at a slightly higher carrier frequency than the 802.11a. Safety related applications of Intelligent Transportation Systems (ITS) have indeed been allocated a 75 MHz bandwidth spanning from 5.850 GHz to 5.925 GHz (whereas the IEEE 802.11a operates in the $5.170 - 5.230$ GHz and $5.735 - 5.835$ GHz bands), which is free of interference from competing wireless devices, hence enabling fast and reliable real-time communications between vehicles on the road,

- Uses a 10 MHz bandwidth, in order to make signal more robust against fading (rather than a 20 MHz one in the IEEE 802.11a). As a consequence, all timing parameters are doubled compared to the 20 MHz case, i.e. the robustness against delay spread is increased (due to a doubled cyclic prefix length), but the one against Doppler spread is reduced (due to a halved subcarrier frequency spacing). On the other hand, note that this also implies that the corresponding data rates are reduced.

A side-by-side comparison of the PHY layer parameters of the IEEE 802.11p standard and the ones of the IEEE 802.11a standard is provided in Table 5.1.

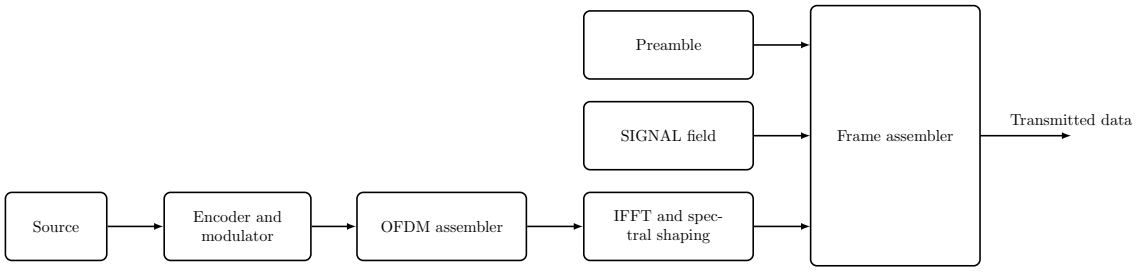

Figure 5.1: Block diagram of the Transmitter

5.1.2 At the Transmitter side

In this Section, we present all the steps that are applied on the binary data stream intended for transmission over the radio propagation channel. Each of them corresponds to a certain block of the diagram in Fig. 5.1.

5.1.2.1 Data source

The number of generated random bits is given as

$$N = N_{\text{SD}} \cdot N_{\text{sym}} \cdot R \cdot N_{\text{BPSC}}, \tag{5.1}$$

where N_{SD} is the number of data subcarrier ($N_{\text{SD}} = 48$ for the IEEE 802.11p), N_{sym} the number of OFDM data symbols per frame, R the coding rate and N_{BPSC} the number of bits (corresponding to one constellation point), respectively.

5.1.2.2 Encoder, interleaver and mapper

Scrambler: The transmitted bits are scrambled in order to randomize the data pattern, hence avoiding long sequences of bits of the same value. The dependence of a signal's power spectrum upon the actual transmitted data is therefore eliminated. The frame synchronous scrambler uses a generator polynomial $S(x)$ which is defined as

$$S(x) = x^7 + x^4 + 1. \tag{5.2}$$

The scrambler is implemented as a shift register consisting of 7 delays and 2 modulo-2 adders, as shown in Fig. 5.2. It repeatedly generates a 127-bit sequence with 1011101 as initial state. The output of the scrambler is a modulo-2 sum of the scrambling sequence and the data.

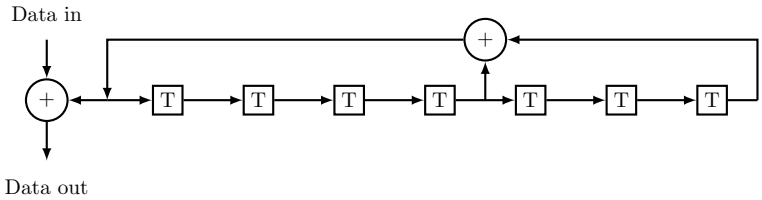

Figure 5.2: Data scrambler

Encoder: The scrambled data are then passed to a convolutional encoder in order to introduce some redundancy into the data stream. This redundancy is used at the Rx side as error correcting

coding for mitigating the fading and/or noise effects affecting the signal during the transmission over the radio propagation channel.

Convolution codes are defined by three main parameters, namely *(i):* the number of input bits k, *(ii):* the number of output bits n and *(iii):* the number of memory register m. The number of information bits that potentially influence a given code bit is defined by so-called constraint length of a convolutional encoder, given as $K = m + 1$. The encoder uses the industry-standard coding rate $R = 1/2$, i.e. at each time index the encoder takes $k = 1$ information bit as input and produces $n = 2$ code bits at its output. This corresponds to the two generator polynomials $g_0 = 133_8 = [0\,1\,0\,1\,1\,0\,1\,1]_2$ and $g_1 = 171_8 = [0\,1\,1\,1\,1\,0\,0\,1]_2$ (where the binary 1s indicate the connections), as shown in Fig. 5.3.

Moreover, higher codes rates ($R = 2/3$ and $R = 3/4$) can be obtained by puncturing, which consists in periodically deleting certain bits in the reference code sequence. The output elements are selected according to a puncture vector: the k^{th} reference code rate element of the input vector will be represented in the output vector (resp. removed) if the k^{th} element of puncture vector is one (resp. zero). Two puncture vectors $p_0 = [1\ 1\ 1\ 0]$ and $p_1 = [1\ 1\ 0\ 1\ 1\ 0]$ are used in order to achieve rates $R = 2/3$ and $R = 3/4$, respectively.

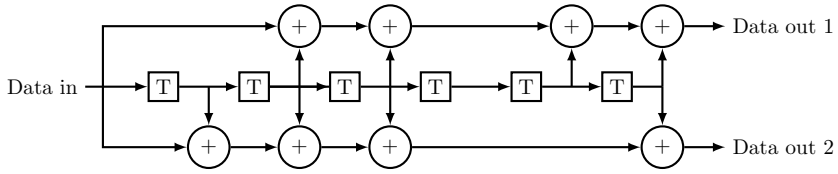

Figure 5.3: Data encoder

Interleaver: When too many errors appear in a block of data (e.g. due to fading, noise, etc.), the decoding cannot be done correctly. To reduce the effects of burst errors, the coded data are rearranged such that consecutive data are split among different blocks. Hence, the source of burst errors appears to be statistically independent at the output of the interleaver, allowing therefore better error correction at the Rx side.

The interleaving in the PHY layer of the IEEE 802.11p standard is defined as a two-step permutation: the first permutation ensures that adjacent coded bits are mapped onto non-adjacent subcarriers, while the second ensures that adjacent coded bits are mapped alternately onto less and more significant bits of the constellation. The interleaver operates on blocks of N_{CBPS} encoded data bits, which is the number of bits in a single OFDM symbol as given in Table 5.2.

Let k denotes the index of the bit before the first permutation, i the index after the first permutation and before the second permutation, and j the index of second permutation, just prior to modulation. The first permutation is defined as

$$i = \frac{N_{\text{CBPS}}}{16}\ (k \bmod 16) + \left\lfloor \frac{k}{16} \right\rfloor, \quad k = 0, 1, \ldots, N_{\text{CBPS}} - 1, \tag{5.3}$$

where $\lfloor \cdot \rfloor$ is the ceiling function. Note that this operation corresponds to writing the input bits into a matrix with 16 columns and a variable number of rows (which depends on the modulation scheme). The output bits are obtained by reading the matrix column by column. The second permutation is defined as

$$j = s \left\lfloor \frac{i}{s} \right\rfloor + \left(i + N_{\text{CBPS}} - \frac{16i}{N_{\text{CBPS}}} \right) \bmod(s), \quad i = 0, 1, \ldots, N_{\text{CBPS}} - 1, \tag{5.4}$$

Modulation	Coding rate (R)	Coded bits per subcarrier (N_{BPSC})	Coded bits per OFDM symbol (N_{CBPS})	Data bits per OFDM symbol (N_{DBPS})	Data rate (Mb/s)
BPSK	1/2	1	48	24	3
BPSK	3/4	1	48	36	4.5
QPSK	1/2	2	96	48	6
QPSK	3/4	2	96	72	9
16BPSK	1/2	4	192	96	12
16QAM	3/4	4	192	144	18
64QAM	2/3	6	288	192	24
64QAM	3/4	6	288	216	27

Table 5.2: Modulation-dependent parameters

where $s = \max(N_{\text{BPSC}}/2, 1)$ is a parameter which is determined by the number N_{BPSC} of coded bits per subcarrier. Note that this operation corresponds to changing the position of the input bits according to the elements vector.

Subcarrier modulation mapping: The encoded and interleaved binary serial input data are divided into groups of N_{BPSC} bits and converted into complex numbers representing BPSK, QPSK, 16-QAM or 64-QAM constellation points, according to the Gray-coded constellation mappings shown in Fig. 5.4. The output values are multiplied by a normalization coefficient K_{MOD} in order to achieve equal average symbol power for all mappings, i.e.

$$S = (S_I + jS_Q) \cdot K_{\text{MOD}}, \tag{5.5}$$

where K_{MOD} depends on the modulation mode: $K_{\text{MOD}} = 1, 1/\sqrt{2}, 1/\sqrt{10}$ and $1/\sqrt{42}$ for BPSK, QPSK, 16-QAM or 64-QAM, respectively.

5.1.2.3 OFDM symbol assembler

As already mentioned above, 64 OFDM subcarriers are used for the signal transmission. The OFDM symbols are created by dividing the serial stream of complex data at the output of the modulator into groups of $N_{\text{SD}} = 48$ complex numbers (corresponding to the number of data subcarriers) and are logically numbered from 0 to 47. These logical subcarrier numbers are then mapped into frequency offset index -26 to 26, where

- four pilot subcarriers are inserted into positions -21, -7, 7 and 21. They contain signal values which are known at the Rx side and used for *(i):* coherent detection robust against the frequency offset and phase noise, and *(ii):* preserving the orthogonality of the subcarriers (by ensuring accurate frequency and time synchronization),
- the zero DC subcarrier is not used since it can cause carrier feedthrough in the RF system as well as problems in the ADC and DAC,
- the subcarriers -32 to -27 and 28 to 32 are all set to zero, hence forming a guard band that considerably contributes in reducing the out of band power.

The subcarrier allocation within each OFDM symbol is summarized in Fig. 5.5.

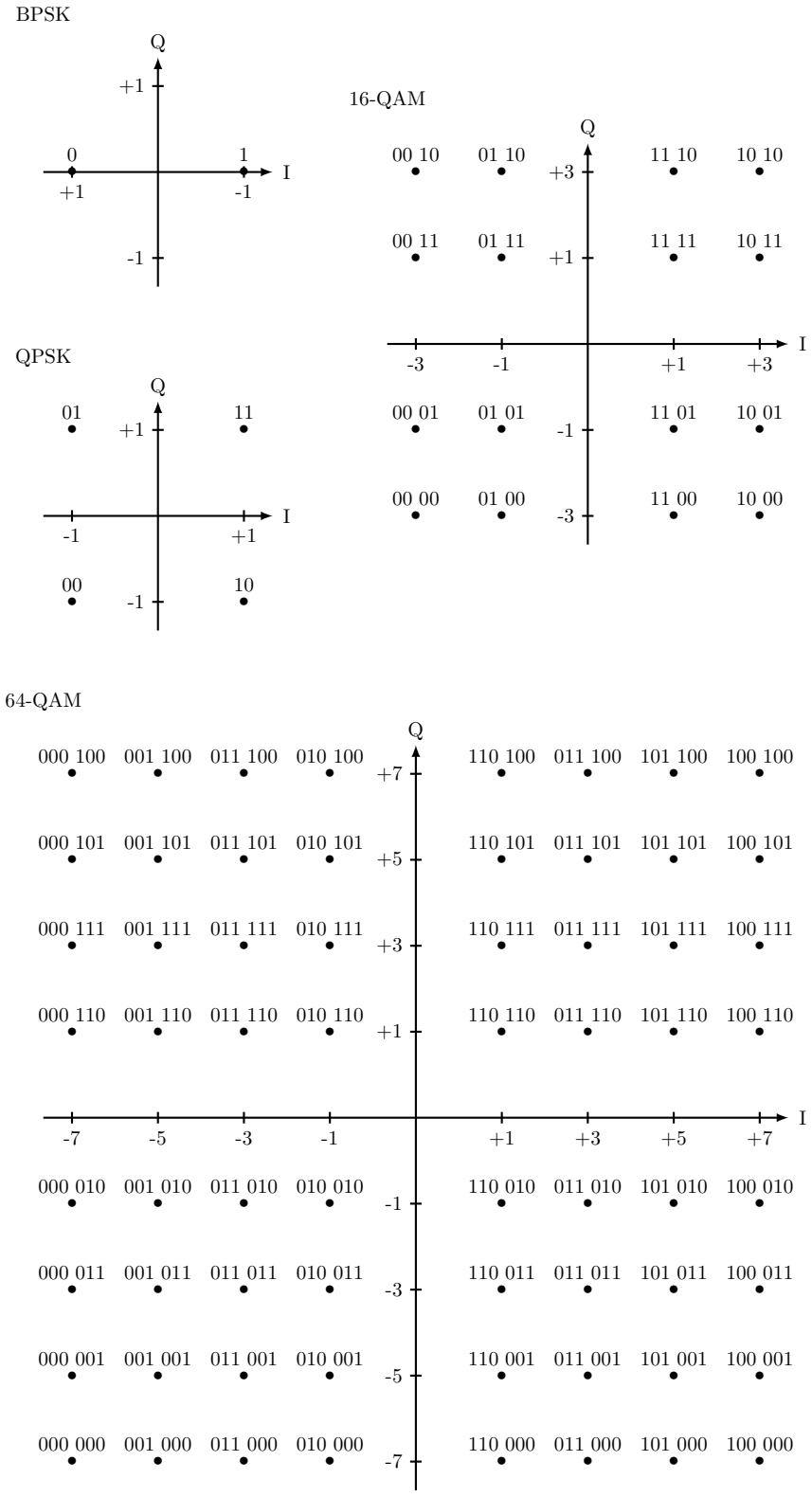

Figure 5.4: BPSK, QPSK, 16-QAM and 64-QAM constellation bit encoding

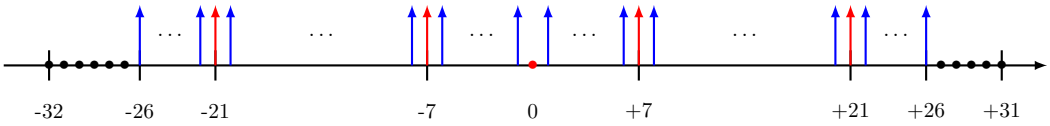

Figure 5.5: Subcarrier allocation of the OFDM symbol

5.1.2.4 IFFT and spectral shaping

An OFDM system considers the symbols containing transmit data as if they are in the frequency-domain. As a consequence, an Inverse Fast Fourier Transform (IFFT) operation is necessary in order to convert the complex data stream back into the time-domain before transmission over the radio propagation channel. Prior to performing the IFFT operation, the subcarriers are to be rearranged as follows: the coefficients 0 to 31 are mapped to the same numbered IFFT inputs, whereas the coefficients -32 to -1 are copied into IFFT inputs 32 to 63. This IFFT operation takes in K modulated symbols, as given by Eq. (5.5), at a time and its output are the corresponding time-domain samples given by

$$s\left[n\right] = \frac{1}{\sqrt{K}} \sum_{k=0}^{K-1} S\left[k\right] e^{j2\pi \frac{kn}{K}}, \tag{5.6}$$

where $K = 64$ denotes the total number of subcarriers of the system, whereas $S\left[k\right]$ is the amplitude and phase of the modulated symbol of the k^{th} subcarrier. After the transformation in time-domain is completed each OFDM symbol is preceded by a periodic extension of itself, thus forming the cyclic prefix, whose duration is given by

$$T_{\text{CP}} = \frac{T_{\text{FFT}}}{4}, \tag{5.7}$$

where T_{FFT} corresponds to the Fast Fourier Transform (FFT) period, which is defined in Table 5.1. In other words, the cyclic prefix is a copy of the 16 last time samples being inserted at the beginning of the OFDM symbols, in order to mitigate the effect of inter-symbol interference due to the multipath propagation, by converting the linear convolution with the channel impulse response to a circular convolution, which can subsequently be equalized by the receiver in a simple fashion. The total length of an OFDM symbol is therefore $T_{\text{SYM}} = T_{\text{FFT}} + T_{\text{CP}} = 8\mu$s.

Smoothing the transitions between consecutive OFDM symbols is also required in order to reduce the spectral sidelobes of the transmitted waveform. The boundaries of each OFDM symbol are set by multiplication by a time-windowing function, which is defined as a rectangular pulse with duration $T_{\text{WF}} = T_{\text{WF}} + T_{\text{TR}}$, where $T_{\text{TR}} = 100$ns is a transition time. It slightly exceeds the length of an OFDM symbol, hence creating a small overlap between consecutive OFDM symbols, as shown in Fig. 5.6. The windowing function is defined in discrete-time

$$W\left[k\right] = \begin{cases} 1/2, & k = \{0, 80\}, \\ 1, & 1 \leq k \leq 79, \\ 0, & \text{otherwise} \end{cases} \tag{5.8}$$

where k is the serial number of the sample in time-domain. Finally, an OFDM symbol consists of 81 samples: the 17 first ones corresponds to the cyclic prefix, whereas the rest is a time-domain version of the 64 subcarriers. Moreover, the first and the last sample of each OFDM symbol are halved and summed up with the last sample of the preciding and first sample of the succeeding OFDM symbols respectively, in order to create a 100ns overlap between consecutive symbols.

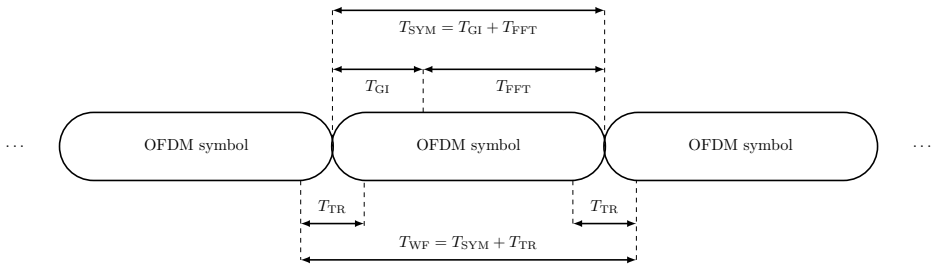

(a) Single reception

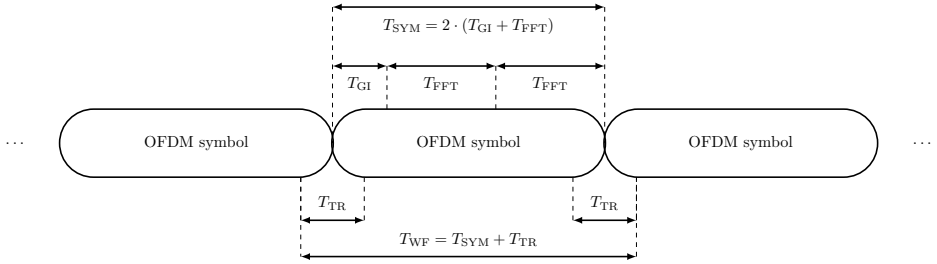

(b) Two receptions of the FFT period

Figure 5.6: OFDM frame with cyclic extension and windowing

5.1.2.5 Constructing PPDU frame

During the transmission, the PSDU shall be appended by a PLCP preamble and a header in order to form the PPDU frame. As shown in Fig. 5.7, the format for the PPDU includes the OFDM PLCP preamble, the OFDM PLCP header, the PSDU, tail bits and pad bits, respectively.

OFDM PLCP Preamble: It is used at the Rx side for synchronization and channel estimation. The OFDM training structure is shown in Fig. 5.8 and consists of

- ten short OFDM training symbols, which are used at the Rx side for synchronization, coarse frequency offset estimation and channel estimation. Each of them consists of 12 subcarriers, which are modulated by the elements of the sequence

$$\begin{aligned} S_{-26,26} = \sqrt{(13/6)}\,\{&0\,,0\,,1+j\,,0\,,0\,,0\,,-1-j\,,0\,,0\,,0\,,1+j\,,0\,,0\,,\\ &0\,,-1-j\,,0\,,0\,,0\,,-1-j\,,0\,,0\,,0\,,1+j\,,0\,,0\,,0\,,\\ &0\,,0\,,0\,,0\,,-1-j\,,0\,,0\,,0\,,-1-j\,,0\,,0\,,0\,,1+j\,,\\ &0\,,0\,,0\,,1+j\,,0\,,0\,,0\,,1+j\,,0\,,0\,,0\,,1+j\,,0\,,0\}\,, \end{aligned} \tag{5.9}$$

  where the coefficient $\sqrt{(13/6)}$ normalizes the average power of the resulting OFDM symbol, which utilizes 12 out of 52 subcarriers. The single period of the short training sequence is then extended periodically for 161 samples and multiplied by the window function

$$W\left[k\right] = \begin{cases} 1/2, & k = \{0, 160\}\,, \\ 1, & 1 \leq k \leq 159, \\ 0, & \text{otherwise}. \end{cases} \tag{5.10}$$

  As a result, the training sequence S in Eq. (5.9) yields ten short OFDM training symbols (denoted t_1 to t_{10} in Fig. 5.8), whose duration is 1.6μs,

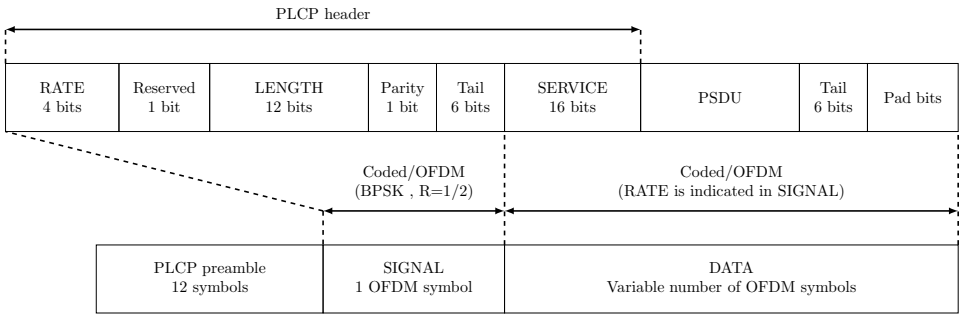

Figure 5.7: PPDU frame format

- two long OFDM training symbols, which are used at the Rx side for fine synchronization as well as improved frequency offset and channel estimation. Each of them consists of 53 subcarriers (including a zero value at DC) which are modulated by the elements of the sequence

$$\begin{aligned} L_{-26,26} = \{&1\ ,1\ ,-1\ ,-1\ ,1\ ,1\ ,-1\ ,1\ ,-1\ ,1\ ,1\ ,1\ ,1\ ,\\ &1\ ,1\ ,-1\ ,-1\ ,1\ ,1\ ,-1\ ,1\ ,-1\ ,1\ ,1\ ,1\ ,1\ ,\\ &0\ ,1\ ,-1\ ,-1\ ,1\ ,1\ ,-1\ ,1\ ,-1\ ,1\ ,-1\ ,-1\ ,-1\ ,\\ &-1\ ,-1\ ,1\ ,1\ ,-1\ ,-1\ ,1\ ,-1\ ,1\ ,-1\ ,1\ ,1\ ,1\ ,1\}\,. \end{aligned} \tag{5.11}$$

  The single period of the long training sequence is then extended periodically and multiplied by the window function defined in Eq. (5.10). This yields two long OFDM training symbols (denoted T_1 and T_2 in Fig. 5.8), each with duration 6.4μs. They are then appended with a cyclic prefix (in order to reduce inter-symbol interferences) of duration $2 \cdot 1.6 = 3.2\mu$s, which is doubled compared to the duration of the cyclic prefix of OFDM data symbols (because it is appended only once in front of the first long OFDM training symbol T_1 and contributes to both T_1 and T_2).

The total training length is therefore of 32μs. Note that three different kinds of guard intervals are defined, namely *(i):* for the short training sequence ($= 0\mu$s), *(ii):* for OFDM data symbols ($= T_{\mathrm{GI}} = 1.6\mu$s), and *(iii):* for the long training sequence ($= 2 \cdot T_{\mathrm{GI}} = 3.2\mu$s).

SIGNAL field: The OFDM training symbols of the PLCP preamble are followed by the SIGNAL field, which purveys the information for decoding the DATA part of the frame. As shown in Fig. 5.7, it consists of a single OFDM symbol, where

- the RATE field has four bits and conveys information about the modulation scheme and the coding rate as used in the rest of the packet, according to Table 5.2,
- the LENGTH field is an unsigned 12-bit integer that indicates the number of octets in the PSDU that the MAC is currently requesting the PHY to transmit. This value is used by the PHY to determine the number of octet transfers that will occur between the MAC and the PHY after receiving a request to start transmission,
- the reserved bit is intended for future use and is set to zero. The even parity (positive parity) bit controls the integrity of the RATE and LENGTH fields. The TAIL field has six bits (also all set to zero) and facilitates a reliable and timely detection the RATE and LENGTH fields immediately after the reception of the tail bits.

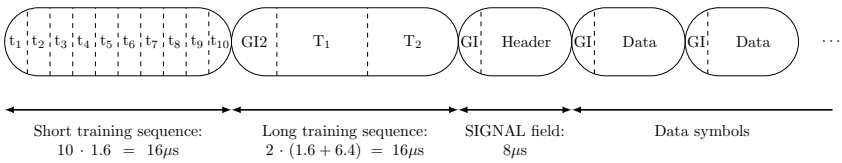

Figure 5.8: OFDM training structure

The encoding of the SIGNAL field is performed using the most robust combination of BPSK modulation of the subcarriers and a coding rate of $R = 1/2$. This includes modulation using IFFT, cyclic extension and multiplication by a window function, as described in Section 5.1.2.4 for OFDM symbols. Moreover, note that the RATE and LENGTH fields are both required for decoding the DATA part of the packet.

DATA field: As shown in Fig. 5.7, the PLCP preamble and the SIGNAL field are finally followed by the DATA field, which contains

- the SERVICE field has 16 bits, all set to zero: bits 0 to 6 are used for synchronization of the descrambler at the Rx side, while bits 7 to 15 are reserved for future use,
- the PPDU TAIL field shall be six bits of zero, which are required to return the convolutional encoder to the zero state. The PLCP tail bit field are produced by replacing six scrambled zero bits following the message end with six non-scrambled zero ones,
- pad bits which ensure that the number of bits in the DATA field is a multiple of the number N_{CBPS} of coded bits in an OFDM symbol, see Table 5.2. To achieve that, the length of the message is extended so that it becomes a multiple of the number N_{DBPS} of data bits per OFDM symbol. At least 6 bits are appended to the message in order to accommodate the TAIL bits. The number N_{SYM} of OFDM symbols, the number N_{DATA} of bits in the DATA field and the number N_{PAD} of pad bits are computed from the length of the PSDU LENGTH field as follows

$$\begin{aligned} N_{\text{SYM}} &= \lceil (16 + 8 \cdot \text{LENGTH} + 6) / N_{\text{DBPS}} \rceil , \\ N_{\text{DATA}} &= N_{\text{SYM}} \cdot N_{\text{DBPS}}, \\ N_{\text{PAD}} &= N_{\text{DATA}} - (16 + 8 \cdot \text{LENGTH} + 6) , \end{aligned} \tag{5.12}$$

  where $\lceil \cdot \rceil$ is the ceiling function. The appended bits are set to zeros and are subsequently scrambled with the rest of the bits in the DATA field.

The SERVICE field of the PLCP header, the PSDU, the six zero tail bits and the pad bits appended are transmitted at the data rate described in the RATE field of SIGNAL and may constitute multiple OFDM symbols. Finally, the PPDU frame can be assembled by simply appending the train of training symbols (i.e. the PLCP preamble), the SIGNAL field (i.e. the information on the transmission setting) and the OFDM data symbols one after another, as shown in Fig. 5.7.

5.1.3 At the Receiver side

In Section 5.1.2, we have described the different steps that are performed at the Tx side in order to transform a binary data stream into OFDM frames (each consisting of a preamble and a payload, respectively) before wireless transmission over the radio propagation channel. At the Rx side, the channel coefficients are first estimated from the preamble and thereafter the processing performed at the Tx side is reversed in a block-wise manner, as shown in Fig. 5.9.

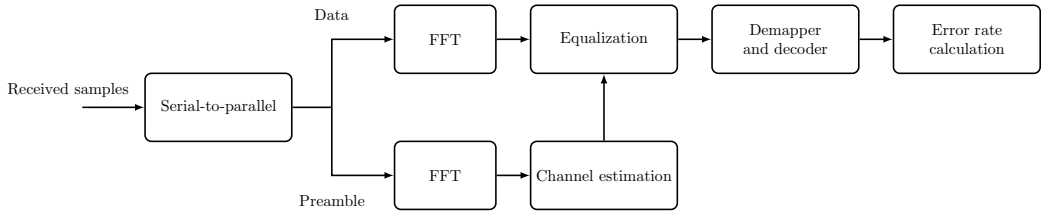

Figure 5.9: Block diagram of the receiver

5.1.3.1 Demodulator

The received signal consists of consecutive PPDU frames, with structure as shown in Figs. 5.7 and 5.8. Each frame is first processed by a demultiplexer (i.e. a serial-to-parallel block), which divides the received signal into blocks of 80 samples: the two first ones correspond to the short training symbols, the two next ones are the long training symbols, the fifth one is the SIGNAL field and the rest are data symbols.

The cyclic prefix is removed by ignoring the 16 first samples inserted at the beginning of each OFDM data symbol. The 64 remaining samples are then demodulated in order to convert them back from the time-domain into the frequency-domain, by means of an FFT operation

$$S\left[k\right] = \frac{1}{\sqrt{K}} \sum_{n=0}^{K-1} s\left[n\right] e^{j 2\pi \frac{nk}{K}}, \tag{5.13}$$

which yields 64 parallel subcarriers. Note that this operation is the reciprocal of the IFFT one in Eq. (5.6) used for the modulation of the data from the frequency to the time-domain.

5.1.3.2 Channel estimation

The cyclically extended guard interval transforms the linear convolution operation between the transmitted data and the channel into a circular convolution one. As a consequence, the frequency-selective channel is converted into narrowband (scalar) sub-channels on parallel subcarriers in the frequency-domain. In that case, the received signal on the k^{th} subcarrier at discrete time instant n is given by

$$r_k\left[n\right] = H_k\left[n\right] s_k\left[n\right] + v_k\left[n\right]. \tag{5.14}$$

The Least Square (LS) estimate $\hat{H}_k\left[n\right]$ of the channel coefficients on the k^{th} subcarrier can be estimated at the Rx side from an ***a priori*** known transmitted sample $s_k\left[n\right]$ and the corresponding received sample $r_k\left[n\right]$ as

$$\hat{H}_k\left[n\right] = \frac{r_k\left[n\right]}{s_k\left[n\right]} = H_k\left[n\right] + \frac{v_k\left[n\right]}{s_k\left[n\right]}. \tag{5.15}$$

where $H_k\left[n\right]$ corresponds to the true channel coefficient and $v_k\left[n\right]/s_k\left[n\right]$ the residual noise, respectively. The main advantages of this method are that it has a low complexity (only a division operation is involved) and requires no prior knowledge of the channel statistics, although at the expense of a possible high mean-square error.

The two long training symbols can be used for that purpose, whose LS estimates are first calculated independently and then averaged in order to obtain the final channel estimate for the k^{th} subcarrier used for subsequent OFDM data symbols, such that

$$\hat{H}_k[n] = \frac{1}{2}\left(\hat{H}_{k,(1)}[n] + \hat{H}_{k,(2)}[n]\right). \tag{5.16}$$

Note that this operation is done on the long training symbols rather than on the short ones. The reason for this is that these latter consist of only 12 non-zero pilots, remember their structure Eq. (5.9), implying therefore that *(i):* only the corresponding channel coefficients can be estimated, and *(ii):* division by zeros in Eq. (5.15) would lead to implementation problems.

5.1.3.3 Equalization

The distortions introduced by the channel to the transmitted signal (e.g. Inter-Symbol Interference (ISI), etc.) can be mitigated with a Zero-Forcing (ZF) equalizer, by applying the inverse of the channel coefficients to the received data symbols. In case when perfect Channel State Information (CSI) is assumed, i.e. all channel coefficients $H_k[n]$ are known at the Rx side, the ZF equalizer can be written as

$$\hat{r}_k[n] = \frac{1}{H_k[n]} r_k[n] = \frac{1}{H_k[n]}\left(H_k[n]\, s_k[n] + v_k[n]\right) = s_k[n] + \frac{v_k[n]}{H_k[n]}. \tag{5.17}$$

The output of the equalizer is given by the transmitted sequence $s_k[n]$ plus a noise component $\tilde{v}_k[n] = v_k[n]/H_k[n]$. However, the main disadvantage of the ZF equalizer is that the noise component can be significantly amplified for small values of channel coefficients, hence resulting in a degradation of the SNR. In practice, the channel coefficients $H_k[n]$ can never be perfectly known at the Rx side. The equalization process is therefore based on their estimates $\hat{H}_k[n]$, which are obtained from the long training symbols as described in Section 5.1.3.2.

5.1.3.4 Demapper, deinterleaver and decoder

Demapper: The complex coded symbols obtained at the output of the equalizer are then demapped into the corresponding binary word, hence inverting the bit to symbol transformation described in Section 5.1.2.2. For that purpose, two different approaches can be considered, namely

- hard demapping, where the detected symbol $\hat{a}[n]$ minimizes the Euclidian distance between the complex received symbol $r[n]$ and all the symbols $a \in \mathcal{A} = \left\{a^{(1)}, a^{(2)}, \ldots, a^{(M_a)}\right\}$ of the constellation used for data transmission (M_a being the length of the symbol alphabet). The decision rule can be written as

$$\hat{a}[n] = \arg\min_{a\in\mathcal{A}} |r[n] - a| = \arg\min_{a\in\mathcal{A}} \sqrt{\left(r_R[n] - a_R\right)^2 + \left(r_I[n] - a_I\right)^2}, \tag{5.18}$$

- soft demapping, which unlike hard demapping takes also into account the reliability information associated to a given observation. For the i^{th} coded bit a_i ($1 \leq i < M_a$), it is calculated from the complex received symbol $r[n]$ based on the Log-Likelihood Ratio (LLR), which is defined as

$$\begin{aligned} L\left(a_i \,|\, r[n]\right) &= \log \frac{P\left(a_i = 1 \,|\, r[n]\right)}{P\left(a_i = 0 \,|\, r[n]\right)} \\ &= \log \frac{P\left(a_i = 1\right)}{P\left(a_i = 0\right)} + \log \frac{\sum_{a\in\mathcal{A}_{i,1}} P\left(r[n] \,|\, a\right)}{\sum_{a\in\mathcal{A}_{i,0}} P\left(r[n] \,|\, a\right)}, \end{aligned} \tag{5.19}$$

where $\mathcal{A}_{i,1} = \{a \,|\, a_i = 1\}$ and $\mathcal{A}_{i,0} = \{a \,|\, a_i = 0\}$ denote the sets of the $2^{M_a - 1}$ symbols having $a_i = 1$ and $a_i = 0$, respectively. The last equality in Eq. (5.19) follows from Bayes' rule. The sign of the LLR provides information about the value of the coded bit a_i (either $a_i = 1$ or $a_i = 0$), whereas its magnitude measures the reliability of the associated decision. Hence, soft demapping outperforms hard demapping and reduces significantly the probability of residual errors.

Deinterleaver: The coded bits at the output of the demapper are deinterleaved in order to retrieve the original sequence. Hence, the source of burst errors appears to be statistically independent at the Rx side, thus allowing better error correction.

Simular to the interleaver described in Section 5.1.2.2, the deinterleaver is defined by two permutations. Denoting j the index of the original received bit before the first permutation and i the index after the first and before the second permutation, the first permutation is the inverse of the one defined in Eq. (5.4), and is then defined as

$$i = s \cdot \left\lfloor \frac{j}{s} \right\rfloor + j + \left(\frac{16j}{N_{\text{CBPS}}} \right) \bmod(s) \quad , \quad j = 0, 1, \ldots, N_{\text{CBPS}} - 1, \tag{5.20}$$

where s denotes the number of coded bits per subcarrier N_{BPSC}, as defined in Eq. (5.4). The second permutation is given by

$$k = 16i - (N_{\text{CBPS}} - 1) \left\lfloor \frac{16i}{N_{\text{CBPS}}} \right\rfloor \quad , \quad i = 0, 1, \ldots, N_{\text{CBPS}} - 1, \tag{5.21}$$

where k is the index after the second permutation, just before the convolutional decoder. This permutation corresponds to the inverse of the one defined in Eq. (5.3).

Decoder: Since the transmitted signal was punctured in order to increase the coding rate R (see Section 5.1.2.2), some of the encoded bits are missing and have therefore to be compensated. To do so, zeros are inserted at their positions in the received coded bit sequence, i.e. the code rate is converted back to the reference code rate $R = 1/2$.

The IEEE 802.11p standard recommends the Viterbi algorithm for decoding. This algorithm aims at finding the most likely transmitted sequence of symbols $\hat{s}$ given the received sequence of symbols r, such that

$$\hat{s} = \max_{a} P\left(r \,|\, s\right), \tag{5.22}$$

where the maximization is done over all possible symbol sequences s that can be transmitted. It is based on the trellis framework, which makes explicit the time evolution of the content of the shift registers of the convolutional encoder. At each time instant n,

- for a convolutional code with constraint length $K = 7$, there are $2^{K-1} = 64$ nodes of the trellis correspond to all possible states of the encoder (i.e. all possible combinations of bits in its shift registers, as shown in Fig. 5.3),
- the state transitions to the next time instant $n + 1$ are given by the branches of the diagram. Depending on the bit at the input of the encoder (which is either a 0 or a 1), note that each state can reach only two other states, i.e. some state transitions are not possible.

Each path throughout the trellis describes therefore a given sequence of states, which corresponds to a unique sequence of *(i):* bits intended for transmission at the input of the encoder, and *(ii):* the corresponding coded bits at its output, respectively.

The Viterbi algorithm uses two metrics in order to retrieve the input data bits from the coded received ones, namely *(i):* the branch metric and *(ii):* the path metric. The branch metric is defined for each state transition in the trellis and corresponds to the distance between the received coded bits and the expected ones. On the other hand, the path metric is associated with each node of the trellis and indicates the "most likely" path between the initial state and the current one (i.e. associated with the smallest distance), among all possible paths between these two states. In other words, this path is the one which minimizes the total number of bit errors.

Assuming that the Tx is at state s at a given time instant n, it must have been in only one of two possible predecessor states (denoted as α and β, respectively) at the previous time instant $n-1$. The Viterbi algorithm can then be described as follows:

1. Calculate the branch metrics BM $[\alpha \rightarrow s]$ and BM $[\beta \rightarrow s]$ corresponding to the transitions from states α and β to state s, respectively,

2. Add these branch metric to the path metrics for the predecessor state, i.e. PM $[\alpha, n-1]$ and PM $[\beta, n-1]$ for states α and β, respectively. Compare the sums for paths arriving at the new state s and select the one associated with the smallest path value, i.e.

$$\text{PM}\left[s,n\right] = \min\left(\text{PM}\left[\alpha, n-1\right] + \text{BM}\left[\alpha \rightarrow s\right] \text{ , PM}\left[\beta, n-1\right] + \text{BM}\left[\beta \rightarrow s\right]\right), \quad (5.23)$$

3. Discard the other path and repeat Steps 1. and 2. until all received coded bits have been used. The "survivor" path corresponds then to the optimum transmitted bit sequence, i.e. with the smallest path metric (associated with the fewest number of bit errors).

Note that the Viterbi decoder can be used either for hard or soft decoding, depending on the type of decision applied for demapping. For hard decision decoding, the branch and path metrics are calculated with the Hamming distance between the expected bits and the received ones (exploiting the fact that the received data samples have been digitized prior to decoding). Performance can be significantly improved by considering soft decision decoding, which takes into account the knowledge about the reliability of the received bit sequence.

Finally, the decoded data bits are descrambled with the same scrambler as the one used at the Tx side and described in Section 5.1.2.2.

5.2 IEEE 802.11p Medium Access Control layer

The purpose of the MAC layer is, as its name suggests, to control the access to the physical medium (i.e. the propagation channel) for a single wireless device and decide when it can start transmission. However, it has no control on the other nodes of the network and can therefore not prohibit them from sending data packets at the same time. Moreover, note that the way data packets are transmitted over the propagation channel is determined at a lower level by the PHY layer, as described in Section 5.1.2.5.

Each node in the network is indeed independent and must therefore follow a set of distributed rules (algorithms and protocols) in order to determine when and which node can have the right to access to the physical medium (which they all share) and can send a packet. In other words, the MAC layer is responsible for scheduling all channel access while keeping the interference as low as possible at any transmission moment.

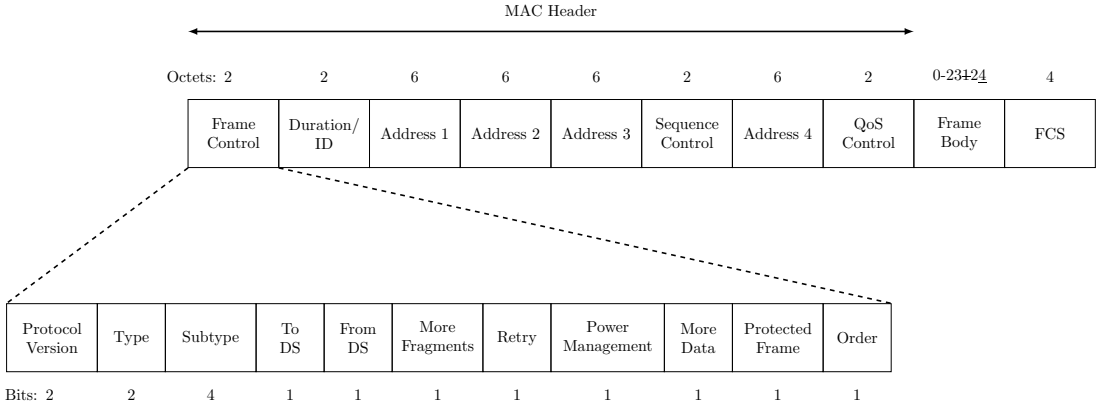

Figure 5.10: MAC frame format

5.2.1 Structure of the MAC frame

MAC frames can be of three different types, namely *(i):* data frames which carry user data from higher layers, *(ii):* control frames which assist in the delivery of data and management frames between stations, including Ready To Send (RTS), Clear To Send (CTS) and Acknowledgment (ACK) frames (see Section 5.2.2), and *(iii):* management frames (e.g. beacons, etc.) which enable stations to establish and maintain communications. Their most general format of the MAC frame is shown in Fig. 5.10 and consists of

A MAC header: The MAC header can have a variety of formats, depending on the type of the frame, which can be *(i):* data frames which carry user data from higher layers, *(ii):* control frames which assist in the delivery of data and management frames between stations, including RTS, CTS and ACK frames (see Section 5.2.2), and *(iii):* management frames (e.g. beacons, etc.) which enable stations to establish and maintain communications. The most common format of the MAC header is shown in Fig. 5.10, with fields

- *Frame control*: This field includes a protocol version, a frame type and subtype, and several other bit fields. The combination of the bits *To DS* and *From DS* defines whether the frame is exchanged between stations within the same Basic Service Set (BSS) or outside. If both bits are set to zero, the frame remains within the same BSS (i.e. on the wireless medium). If the *To DS* bit is set, the Access Point (AP) bridges the frame from the wireless medium to the distribution system. If the *From DS* bit is set, the AP bridges the frame from the distribution system to the wireless medium. The state of these two bits also determines the content of the address fields,

- *Duration / ID*: This field indicates the time duration (in microseconds) required to transmit the current frame, possibly including some overhead for its response (i.e. RTS, CTS and ACK frames) and appropriate Inter Frame Spaces (IFSs). Note that it depends on the type of the frame, Quality of Service (QoS) and address parameters,

- *Addresses* 1, 2, 3 *and* 4: The address field contents are summarized in Table 5.3 for all combinations of *To DS* / *From DS* bit combinations. The general rule is that Addresses 1 and 2 are always associated with the receiving and transmitting addresses, respectively. As a consequence, we can have

  To DS $= 0$ and *From DS* $= 0$: Both the source and destination are on the wireless medium. In that case, Addresses 1, 2 and 3 correspond to the destination, source and Basic Service

To DS bit	*From DS* bit	Address 1	Address 2	Address 3	Address 4
0	0	DA	SA	BSSID	-
0	1	DA	BSSID	SA	-
1	0	BSSID	SA	SA	-

Table 5.3: IEEE 802.11p MAC frame address field content. DA: Destination Address; SA: Source Address; BSSID: Basic Set Service Identification (Access Point Address)

Set Identification (BSSID) addresses, respectively,

To DS $= 0$ and *From DS* $= 1$: When a frame arrives from across the distribution system where it was sent by the source, whereas the access point bridges the frame onto the wireless medium. In that case, the transmitting address identifies the access point. As a consequence, Addresses 1, 2 and 3 correspond to the destination, BSSID (i.e. the MAC address of the access point) and source addresses, respectively,

To DS $= 1$ and *From DS* $= 0$: When a frame is sent over the wireless medium, received by the access point and bridged onto the Delay Spread (DS) toward its final destination. In that case, the receiving address identifies the access point. Hence, Addresses 1, 2 and 3 carry the BSSID (i.e. the MAC address of the access point), the source and destination addresses, respectively,

- *Sequence Control*: This field consists of two sub-fields, the Sequence Number (12 bits) and the Fragment Number (4 bits), which are used to identify the sequence number of a MAC Service Data Unit (MSDU) and the number of each fragment of a MSDU, respectively. Fragmentation may indeed be necessary for partitioning the user data stream from higher layers passed to the MAC layer to meet the maximum allowed size of the MSDU,

- *QoS Control*: This field is used in order to identify the traffic class or traffic stream to which the current frame belongs as well as various other QoS-related information about the frame, depending on its type and subtype (e.g. ACK policy, transmission opportunity (TXOP) duration, queue size, etc.)

A variable-length frame body: The frame body consists of the MSDU, possibly augmented by a few bytes of encryption overhead, which is passed into the MAC layer from an higher layer. Its maximum size is limited to 2304 bytes. It is therefore much smaller than the 4095 bytes of the maximum PSDU allowed by the OFDM PHY layer, as described in Section 5.1.2.5. In practice, typical MAC frames used in the IEEE 802.11p standard are less than 1600 bytes,

A Frame Check Sequence (FCS): It is a 4-byte field which contains a 32-bit Cyclic Redundancy Check (CRC) used for detecting bit errors anywhere in the MAC frame. It is generated with the standard generator polynomial of degree 32 defined as

$$G(x) = x^{32} + x^{26} + x^{23} + x^{22} + x^{16} + x^{12} + x^{11} + x^{10} + x^8 + x^7 + x^5 + x^4 + x^2 + x + 1, \tag{5.24}$$

and is calculated over all the fields of the MAC header and the frame body.

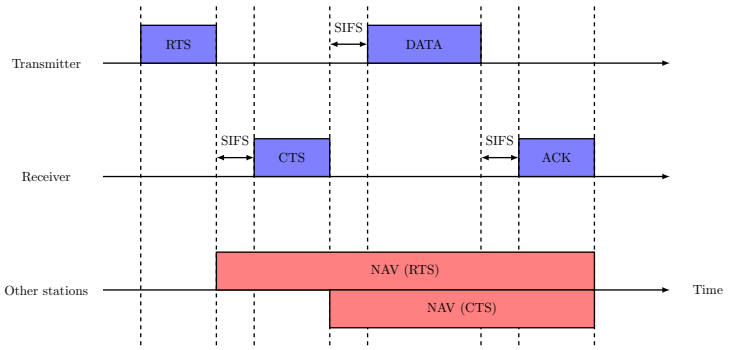

Figure 5.11: RTS/CTS/ACK frame protection sequence with Network Allocation Vector

5.2.2 CSMA/CA

The IEEE 802.11p communication standard uses a Carrier Sense Multiple Access with Collision Avoidance (CSMA/CA) scheme for the coordination of the access to the wireless medium. This mechanism is based on virtual carrier (medium) sensing in order to detect multiple access to the medium. A station may indeed not be allowed to send a data packet if it indicates that the medium is currently occupied by another station.

Fig. 5.11 illustrates the frame exchange sequence of virtual carrier sensing. First, a RTS control frame is sent by the source station, which must be answered by the destination station after Short Inter Frame Space (SIFS) units of time with a CTS frame: the destination node is ready to receive data. The source station waits another SIFS units of time and then sends the data packet. When the destination has received the data successfully, it again waits SIFS units of time before returning an ACK frame. If the source receives the ACK, it will make sure that the data transmission was successful. Otherwise, the source station will continue transmitting the data until it gets a response. In this scenario, all stations within range receive the RTS, the CTS or both frames. When this is the case, they start a Network Allocation Vector (NAV) timer, which marks the medium as busy until the end of the transmission (i.e. the time interval used to transmit the data frame and return its ACK) and prohibits them from sending packets (and therefore interfering) during the current transmission.

5.2.3 Distributed coordination function

Stations operating in the Distributed Contribution Function (DCF) mode always have to wait Distributed Inter Frame Space (DIFS) units of time after a frame (data or control). However, multiple other stations might also have been waiting, i.e. further rules are required to determine which station is going to have first access to the medium for transmission. For that purpose, the time a station must wait after DIFS is uniformly randomized, hence providing fairness between all the stations. The random waiting time is chosen within a range called the Contention Window (CW). The rules for DCF are shown in Fig. 5.12 and can be summarized as follows:

- If a station is newly initialized, then it may send a frame immediately after DIFS units of time if the medium is free. Otherwise, if the medium is not idle, a back-off time is uniform randomly chosen from the interval $[0 \cdots \mathrm{CW}_{\mathrm{min}}]$. Once the medium is idle and DIFS units of time have elapsed, the station must still wait while the back-off counter is decremented for each SlotTime interval. If the medium is seized by another station, the back-off counter stops being decremented. The decrementing process proceeds once the medium is idle again

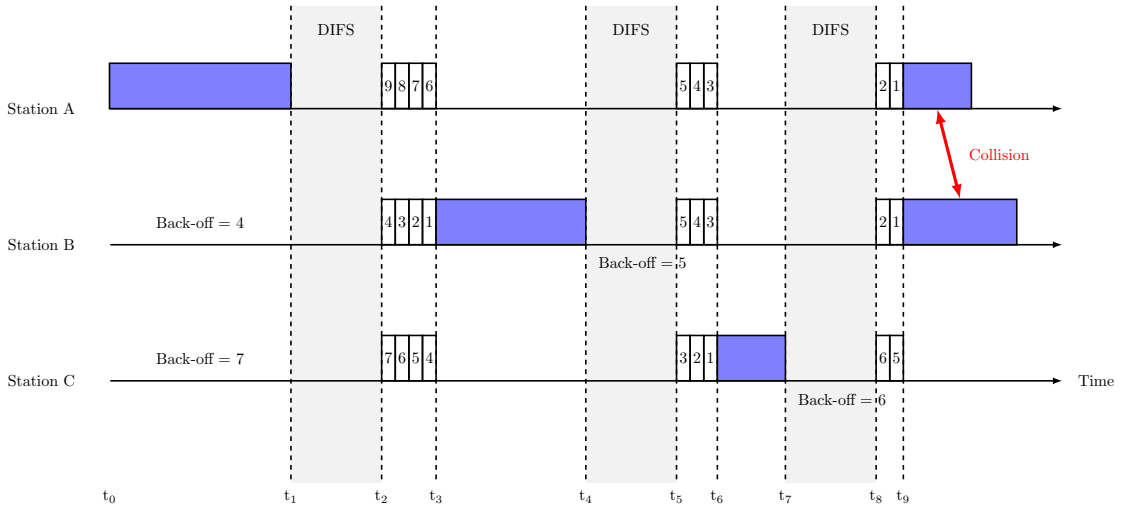

Figure 5.12: Example of back-off coordination between three different stations in DCF. The blue rectangles correspond to a station sending of a packet. DIFS is represented in gray and corresponds to a time interval after a frame during which all stations must wait. Finally, the white rectangles correspond to the decrement of the back-off counter of each station for each SlotTime interval. Note that in this example, a collision between stations A and B may occur at time t_9

Parameters:	SlotTime	SIFS	DIFS	CW_{min}	CW_{max}
Values:	13μs	32μs	32μs	15	1023

Table 5.4: Timing and DCF parameters for the PHY layer of the IEEE 802.11p standard

for DIFS units of time. When the back-off counter reaches zero, the station may send the waiting frame,

- If sending of the frame does not succeed (i.e. if the source station does not receive an ACK answer after a specific timeout), then it must be retransmitted. A further back-off is therefore started, which is randomly selected from an enlarged interval $[0 \cdots \mathrm{CW}]$, where the initial CW is set to $\mathrm{CW}_{\mathrm{min}}$. For subsequent retransmissions, the new CW is determined as

$$\mathrm{CW}_{\mathrm{new}} = \min\left\{2 \cdot (\mathrm{CW}_{\mathrm{old}} + 1) - 1\ ;\ \mathrm{CW}_{\mathrm{max}}\right\}. \tag{5.25}$$

- If the frame transmission was successful, then the station must always start a new back-off procedure, regardless if it has another packet waiting or not.

Note here that DCF does not prohibit collisions, but only avoid them using random back-offs. Moreover, DCF is a statistically fair mechanism for all stations with respect to the time they have to wait before access to the medium. However, it does not take into account the packet payload size or the transmission time of each station, i.e. QoS is not provided. Table 5.4 summarizes the main timing and DCF parameters for the IEEE 802.11p standard.

5.2.4 Enhanced Distributed Channel Access

QoS is however crucial for vehicular communications, where safety-related and time-critical messages must have priority over the other ones. For that purpose, the IEEE 802.11p standard adapts

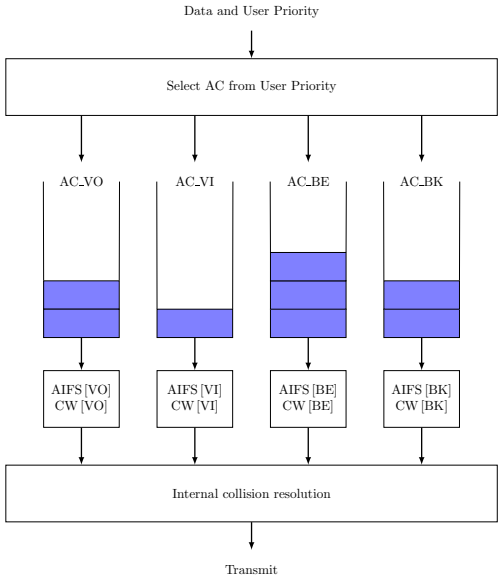

Figure 5.13: EDCA QoS queues

the Enhanced Distributed Channel Access (EDCA) that was originally proposed in the IEEE 802.11e amendment of the standard [38], which introduced a QoS extension. An overview of the EDCA architecture for vehicular communications is shown in Fig. 5.13.

The medium access rules of DCF are replaced by the ones of EDCA, which defines four different Access Categorys (ACs) with different medium access priorities, i.e. *(i):* AC_VO for "voice" class traffic, *(ii):* AC_VI for "video" class traffic, *(iii):* AC_BE for best effort traffic, and *(iv):* AC_BK for background traffic, respectively. Hence, each AC has a separate queue and a Enhanced Distributed Channel Access Function (EDCAF) managing back-off very similar to the original DCF described in Section 5.2.3. The main differences between DCF and EDCA can be summarized as follows:

- The DIFS in DCF is replaced by a specific time interval called Arbitration Inter Frame Space (AIFS) before the EDCAF is granted access to the medium or starts decreasing its back-off counter, which is calculated as follows:

$$\text{AIFS}\,[\text{AC}] = \text{SIFS} + \text{AIFSN}\,[\text{AC}] \cdot \text{SlotTime}, \tag{5.26}$$

  where AIFSN $[\text{AC}]$ is an integer and SlotTime the smallest amount of time that can be added to an IFS, respectively,

- Each AC is defined with a separate CW variable, starting at $\text{CW}_{\text{min}}[\text{AC}]$ and being increased until $\text{CW}_{\text{max}}[\text{AC}]$ is reached,

- When the back-off counter reaches zero, the AC is granted an EDCA TXOP, with a maximum duration TXOPLimit$[\text{AC}]$. A TXOPLimit $= 0$ allows a single frame at any data rate and a RTS/CTS/ACK exchange if desired.

Note that QoS-enabled station has four EDCAFs, i.e. two or more of its back-off counters can reach zero simultaneously. In order to avoid such an internal collision, access to the medium is granted to the EDCAF with the highest priority whereas the other EDCAF must initiate the usual back-off procedure, as if an "external" collision on the medium had been detected.

	VO	VI	BE	BK
AIFSN [AC]	2	3	6	9
CW_{min} [AC]	3	3	7	15
CW_{max} [AC]	7	7	15	1023
TXOPLimit [AC]	0	0	0	0

Table 5.5: Default EDCA parameters using OFDM PHY in the 5 GHz band for the IEEE 802.11p standard

5.3 Performance evaluation

The performance of the PHY layer of the IEEE 802.11p standard depend on the parameter settings and the channel model chosen by the user for the simulations. They are usually characterized in terms of error ratios, two measures of which being

- Bit Error Rate (BER), which compares the transmitted bits with the received ones, obtained after demodulation and decoding. It is defined as the number of bit mismatches between the transmitted and received sequences divided by the total number of transferred bits,
- Frame Error Rate (FER), for which the BER is calculated for each frame. If at least one bit is wrong, then the corresponding frame is considered as erroneous. It is defined as the total number of unsuccessfully detected frames divided by the total number of transmitted frames. This is done by computing the CRC on the received MAC frame (i.e. on the received MAC header and frame body) and comparing it to the one present in the received MAC frame (which has been calculated at the Tx side).

These error ratios are usually expressed as a function of SNR. Performance results obtained for *(i):* the measured V2V propagation channels (see Chapter 2), and *(ii):* the GSCM derived from these measurements (see Chapter 4) will be presented in Chapter 6.

Chapter 6

System simulations

In this Chapter, we evaluate the performance of IEEE 802.11p compliant transceivers in the various scenarios and environments that have been measured in Chapter 3. Performance in terms of both BER and FER results are provided and discussed.

6.1 Simulation settings

6.1.1 IEEE 802.11p parameters

In order to transmit the randomly generated data in the PHY-layer simulator transmission chain IEEE 802.11p standard compliant, we choose a QPSK modulation and a convolutional code with rate of $1/2$. Note that this corresponds to a data rate of 6 Mbps, as described in Table 5.1. The reason for this choice is that this modulation scheme is amongst the most robust ones, i.e. the simulation results obtained for the other less protected schemes will be worse. Moreover, data packets with fixed length of 1000 bytes are assumed to be constantly transmitted. All the simulation parameters are summarized in Table 6.1.

6.1.2 Propagation channel settings

The performance of IEEE 802.11p compliant communication systems were estimated at each time instant from the discrete scatterer contributions reconstructed based on their parameters estimated using the RiMAX algorithm, as described in Chapter 4. A selection combining scheme was used to determine from each MIMO snapshot the single Tx-Rx antenna pair over which they were

	Parameters	Values
IEEE 802.11p:	Modulation mode	QPSK
	Code rate	$1/2$
	Bit rate	6 Mbs
	Packet length	1000 bytes
Channel:	Bandwidth	10 MHz
	MIMO signal duration	$640\mu s$
	Number of MIMO per burst	30
	Rate of bursts	20 Hz
	SNR per bit	6 dB

Table 6.1: Simulation parameters of the IEEE 802.11p communication chain

obtained (i.e. the one for which the IR has the strongest power). Note also that the IRs have to be down-sampled from 15 MHz to 10 MHz, i.e. from the bandwidth over which they were measured to the one over which the IEEE 802.11p standard operates, respectively.

The SNR of a bandlimited, power-constrained radio propagation channel can be defined for a multi-carrier system as

$$\text{SNR}_{\text{ch}} = \frac{P}{N_0 K F}, \tag{6.1}$$

where P is the average signal power and $N_0/2$ is the power spectral density of the Additive White Gaussian Noise (AWGN) channel. K is the total number of subcarriers that are utilized for transmission in the OFDM system, whereas F is the frequency separation between the subcarriers (the product KF corresponding to the total bandwidth B).

However, the PHY layer of the IEEE 802.11p standard specifies that each OFDM symbol consists of $K = 64$ subcarriers out of which twelve are zeros (i.e. the frequency guard interval and the DC frequency), as shown in Fig. 5.5. In other words, $\tilde{K} = 52$ subcarriers are effectively used occupied by the data and pilot subcarriers. As a consequence, the channel is oversampled in the frequency domain and the SNRs of the channel over *(i):* the total bandwidth $B = KF$ and *(ii):* the effectively used bandwidth $\tilde{K}F$ are not equal. They are related as follows

$$\text{SNR}_{\text{ch,[dB]}} = \text{SNR}_{\text{[dB]}} + 10 \log_{10} \frac{\tilde{K}}{K} = \text{SNR}_{\text{[dB]}} - 0.9018, \tag{6.2}$$

where 0.9018 is a correction coefficient accounting for the down-sampling issues in the frequency domain. The received signal $r(t)$ can therefore be modeled as

$$r\left(t\right) = \sum_{l=0}^{L-1} h_i\left(t\right) s\left(t - \tau_i(t)\right) + v\left(t\right), \tag{6.3}$$

where $s(t)$ and $v(t)$ are the transmitted signal and the noise components corresponding to the k^{th} subcarrier at the discrete time instant t, respectively. Based on this definition, AWGN with an arbitrary SNR per bit of 6 dB was added to the transmitted data in all following simulations. All the simulation parameters are summarized in Table 6.1.

6.2 Estimation examples

Due to the time limitations, we have only analyzed a few data subsets that correspond to various scenarios that we want to investigate, and previously described in Section 4.1.5.

Fig. 6.1 shows the time-varying behavior of the BER for the T2T_ObTruck data set, which is described in Section 4.1.5. In this measurement scenario, the Tx and Rx trucks are traveling in convoy in the same direction on a I-5 South freeway, and there is one or two big trucks between the two vehicles. As a consequence, the LOS component is most of the time obstructed (or at least strongly attenuated) by at least one full-length truck (up to two) and the trailer of the measurement vehicle traveling ahead of the other. As it can for example be observed between $t = 4$s and $t = 7$s, this yields to very high levels for the BER, around approximately 0.5, i.e. reliable communication between the Tx and Rx vehicles are in that case not possible.

However, it also shows that when the propagation conditions get better, e.g. from $t = 1$s to $t = 3$s when the LOS between the Tx and Rx trucks becomes temporarily unobstructed, the BER can achieve very good performance, from 10^{-2} to 10^{-5}.

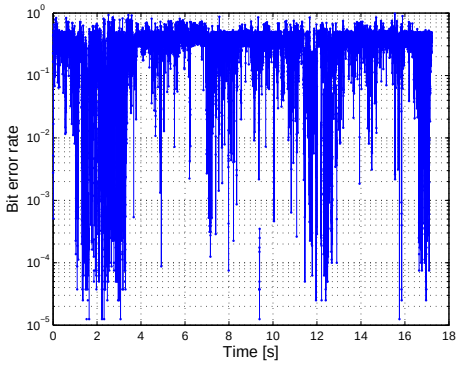

Figure 6.1: Time-varying BER for truck-to-truck communications on a freeway, with the LOS obstructed by other trucks

Chapter 7

Conclusions

7.1 Summary of the project findings

The goal of this project is to investigate the performance of IEEE 802.11p compliant communication systems for interactions of convoys with mixed truck/car situations and assess the impact on convoy formation. This scenarios, in which both trucks and passenger cars are simultaneously on the road, are of great importance for mixed-traffic convoys, but had yet not been explored or measured in the open literature.

For that purpose, we first developed equipment (channel sounder, multiple antenna arrays, etc.) and further refined in order to conduct versatile, mobile measurements of wideband propagation channels. Extensive measurement data sets were therefore obtained for propagation channels between trucks and trucks as well as between trucks and cars in various convoying situations, affecting mixed-passenger-freight traffic, with emphasis on a number of important situations for mixed truck/passenger car traffic with safety-related applications.

Based on these measured data, we showed that the propagation channel can be accurately modeled using a GSCM approach, whose benefits include that *(i):* it can easily handle non-stationary (e.g. fast time-varying) channels, *(ii):* it provides not only delay and Doppler spectra, but inherently models the MIMO properties of the channel, *(iii):* it is possible to easily change the antenna influence, by simply including a different antenna pattern, *(iv):* the environment can be easily changed. The simulation results were found to compare well with the ones obtained from the measured data, and show that the GSCM approach can reliably be used in future system evaluation tools instead of “raw” measurement data.

Finally, we also implemented a simulation platform for the PHY and MAC layers of the IEEE 802.11p standard. This platform was used to evaluate the performance of IEEE 802.11p conforming radios (with “standard” receivers) in such propagation channels. The intrinsic geometry of the trucks (i.e. a large metallic trailer behind the driver’s cabin) is shown to have a significant impact on the evaluation results, when the antennas are mounted on top of the truck driver’s cabin, by *(i):* obstructing the LOS between the Tx and Rx vehicles, with important attenuation, when they are traveling in convoy in the same direction, or *(ii):* acting as a reflector with contribution sometimes stronger than the LOS component located in the near-field of the antennas when both the Tx and Rx vehicles are traveling in opposite directions.

7.2 Implementation outcomes

In this report, we developed and implemented several tools for investigating the performance of IEEE 802.11p compliant communication systems for interactions of convoys with mixed truck/car situations and assess the impact on convoy formation, namely

- A fully functional real-time measurement setup (channel sounder, multiple antenna arrays, etc.) for highly time-varying (vehicle-to-vehicle) propagation channels, which is described in this report,

- A comprehensive database of measured propagation channel characteristics for mixed traffic convoy scenarios. It contains descriptions of the measurement environments, the types of vehicles and their antenna arrangements, distances between the vehicles, LOS/NLOS situations, received powers (as a function of time) and impulse responses, and can be made freely available to the METRANS partners,

- The development of a realistic channel model and its full parametrization, as described in this report. The channel model is coded in MATLAB and can also be made available to the METRANS members,

- The creation of a IEEE 802.11p simulator in MATLAB, which takes into account both the PHY and MAC structures of IEEE 802.11p compliant transmissions. The detailed description of the simulator implementation is described in this report and can also be made available to the METRANS members.

We believe that the tools developed during this project could be used in order to examine more closely the performance of IEEE 802.11p compliant communication systems over realistic propagation channels, in order to improve not only the design of existing control systems but also the development of policies and technologies for convoy formation.

7.3 Future research

Vehicle convoys (platoons) hold a promise for significant efficiency improvements of freight and passenger transportation through better system integration. This research project produced significant results for estimating the characteristics of propagation channels and the performance of IEEE 802.11p compliant communication systems in mixed-traffic convoy scenarios. Based on the obtained results, ongoing and future research should cover the following topics:

- Due to time constraints, only few subsets of measured data have been analyzed during this project, which consisted in the most interesting scenarios. Further work is therefore needed for the exhaustive analysis of all the measurement data collected during the measurement campaigns, in order to test and validate the concepts and tools developed in this project,

- Additional measurement campaigns are required in order to cover additional scenarios (not investigated during this project), for propagation channels between trucks and cars or between trucks and trucks in various convoying scenarios with mixed car/truck traffic. They would indeed include a range of situations important in terms of road safety and convoy formation, e.g. *(i):* in tunnels, *(ii):* at street intersections with truck obstruction, etc.

- Different antenna positions on the vehicles may be alternatively considered, e.g. side mirrors, on top of the trailer, below the vehicles, etc. The performance of IEEE 802.11p compliant communication systems in those cases should be compared to those obtained during this project when the antennas are mounted on the driver's cabin of trucks. The impact of antenna placement on both the characteristics of propagation channels and the performance of communications systems for convoys could then be optimized based on measured data,

- Real-world measurement data indicate that propagation channels between trucks and trucks or between trucks and cars differ significantly from those experienced in (now well-known) car-to-car communication systems. Hence, the proposed GSCM may need to be extended and improved in order to account for *(i):* the presence of a metallic trailer which behaves as a large, strong, constant scatterer (almost in the near-field of the antenna) especially when the Tx and Rx vehicles are traveling in opposite directions towards one another, and *(ii):* the impact of elevation angle, especially for communications between cars and trucks when antennas are located at different heights,

- A more thorough analysis of the packet failure rate, reliabilities and latencies of the wireless links in convoy scenarios is a critically important input for *(i):* the design of control systems, *(ii):* the development of policies and technologies for convoy formation, and *(iii):* possible modifications of the PHY and MAC layers in order to improve the performance of IEEE 802.11p based communication systems in these contexts. In particular, a cross-layer analysis would be interesting to conduct as further work, in order to determine the relationship(s) between the characteristics of system performance, propagation channels and the physical environment surrounding the Tx and Rx vehicles, respectively,

- Based on the results obtained from the measured data, more robust communication schemes can be developed, e.g. by considering multi-hop communications, with other vehicles relaying the information between the Tx and Rx in order to resolve the situations where direct communications are not successful.

Bibliography

[1] R. Kunze, M. Haberstroh, R. Ramakers, K. Henning, and S. Jeschke, Automation, Communication and Cybernetics in Science and Engineering 2009/2010. Springer Berlin Heidelberg, 2011, ch. Automated Truck Platoons on Motorways – A Contribution to the Safety on Roads, pp. 415 – 426, http://dx.doi.org/10.1007/978-3-642-16208-4_38.

[2] S. Tsugawa, "A history of automated highway systems in Japan and future issues," in IEEE International Conference on Vehicular Electronics and Safety (ICVES), Columbus (OH, USA), September 2008, pp. 2 – 3.

[3] S. Shladover, "PATH at 20: History and major milestones," IEEE Transactions on Intelligent Transportation Systems, vol. 8, no. 4, pp. 584 – 592, December 2007.

[4] S I. Stuart Birch, "Mercedes autonomous driving" [Online], https://articles.sae.org/12330.

[5] European Commission, The SATRE project.

[6] "IEEE draft standard for information technology - Telecommunications and information exchange between systems - Local and metropolitan area networks - Specific requirements - Part 11: Wireless LAN medium access control (mac) and physical layer (phy) specifications - Amendment 6: Wireless access in vehicular environments," IEEE Standards Association, February 2010, 10.1109/IEEESTD.2011.5712769.

[7] A. Richter, "Estimation of radio channel parameters: Models and algorithms." ISLE, 2005.

[8] J. Salmi, A. Richter, and V. Koivunen, "Detection and tracking of mimo propagation path parameters using state-space approach," Signal Processing, IEEE Transactions on, vol. 57, no. 4, pp. 1538–1550, 2009.

[9] C. Tan, M. Landmann, A. Richter, L. Pesik, M. Beach, C. Schneider, R. Thomä, and A. Nix, "On the application of circular arrays in direction finding, part ii: Experimental evaluation on sage with different circular arrays," in 1st Annual COST 273 Workshop, no. 5, 2002, pp. 29–30.

[10] "Cylindrical dipole with a quarter-wave balun feed, http://www.antennamagus.com/blog/166/cylindrical-dipole-antenna-with-quarter-wave-balun-feed."

[11] V. Constantinos, C. Vasilis, and K. Panos, "Geometry aspects and experimental results of a printed dipole antenna," Int'l J. of Communications, Network and System Sciences, vol. 2010, 2010.

[12] "Computer Simulation Technology Microwave Studio, https://www.cst.com/products/cstmws."

[13] I. Sen and D. W. Matolak, "Vehicle-vehicle channel models for the 5 GHz band," IEEE Transactions on Intelligent Transportation Systems, vol. 9, no. 2, pp. 235 – 245, June 2008.

[14] O. Renaudin, V. M. Kolmonen, P. Vainikainen, and C. Oestges, "Wideband MIMO car-to-car radio channel measurements at 5.3 GHz," in IEEE 68th Vehicular Technology Conference (VTC), Calgary (Canada), September 2008.

[15] A. Paier, J. Karedal, N. Czink, C. Dumard, T. Zemen, F. Tufvesson, A. F. Molisch, and C. F. Mecklenbräuker, "Characterization of vehicle-to-vehicle radio channels from measurements at 5.2 GHz," Wireless Personal Communications, vol. 50, no. 1, pp. 19 – 32, January 2009.

[16] J. Kunisch and J. Pamp, "Wideband car-to-car radio channel measurements and model at 5.9 GHz," in IEEE 68th Vehicular Technology Conference (VTC), Calgary (Canada), September 2008.

[17] G. Acosta-Marum and M. A. Ingram, "Six time- and frequency-selective empirical channel models for vehicular wireless LANs," in IEEE 66th Vehicular Technology Conference (VTC), Baltimore (MD, USA), September 2007.

[18] L. Cheng, B. E. Henty, D. D. Stancil, F. Bai, and P. Mudalige, "Mobile vehicle-to-vehicle narrow-band channel measurement and characterization of the 5.9 GHz Dedicated Short Range Communication (DSRC) frequency band," IEEE Journal on Selected Areas in Communications, vol. 25, no. 8, pp. 1501 – 1516, October 2007.

[19] A. Paier, L. Bernadó, J. Karedal, O. Klemp, and A. Kwoczek, "Overview of vehicle-to-vehicle radio channel measurements for collision avoidance applications," in 71st IEEE Vehicular Technology Conference (VTC), Taipei (Taiwan), May 2010, pp. 1 – 5.

[20] A. F. Molisch, F. Tufvesson, J. Karedal, and C. F. Mecklenbräuker, "A survey on vehicle-to-vehicle propagation channels," IEEE Transactions on Wireless Communications, vol. 16, no. 6, pp. 12 – 22, December 2009.

[21] C. F. Mecklenbräuker, A. F. Molisch, J. Karedal, F. Tufvesson, A. Paier, L. Bernadó, T. Zemen, O. Klemp, and N. Czink, "Vehicular channel characterization and its implications for wireless system design and performance," Proceedings of the IEEE, special issue on Vehicular Communications, vol. 99, no. 7, pp. 1189 – 1212, July 2011.

[22] A. J. Rustako, M. J. Gans, G. J. Owens, and R. S. Roman, "Attenuation and diffraction effects from truck blockage of an 11-GHz line-of-sight microcellular mobile radio path," IEEE Transactions on Vehicular Technology, vol. 40, no. 1, pp. 211 – 215, February 1991.

[23] A. Yamamoto, K. Ogawa, T. Horimatsu, A. Kato, and M. Fujise, "Path-loss prediction models for intervehicle communication at 60 GHz," IEEE Transactions on Vehicular Technology, vol. 57, no. 1, pp. 65 – 78, January 2008.

[24] T. Abbas, K. Sjöberg, J. Karedal, and F. Tufvesson, "Measurement based shadow fading model for vehicle-to-vehicle network simulations," CoRR, vol. abs/1203.3370, October 2012, http://arxiv.org/abs/1203.3370.

[25] L. Bernadó, T. Zemen, F. Tufvesson, A. F. Molisch, and C. F. Mecklenbräuker, "Delay and Doppler spreads of non-stationary vehicular channels for safety relevant scenarios," IEEE Transactions on Vehicular Technology, vol. 63, no. 1, pp. 82 – 93, January 2014.

[26] M. Boban, R. Meireles, J. Barros, O. Tonguz, and P. Steenkiste, “Exploiting the height of vehicles in vehicular communication,” in IEEE Vehicular Networking Conference (VNC), Amsterdam (The Netherlands), November 2011, pp. 163 – 170.

[27] R. He, A. F. Molisch, F. Tufvesson, Z. Zhong, B. Ai, and T. Zhang, “Vehicle-to-vehicle propagation models with large vehicle obstructions,” IEEE Transactions on Intelligent Transportation Systems, vol. 15, no. 5, pp. 2237 – 2248, April 2014.

[28] J. Karedal, F. Tufvesson, N. Czink, A. Paier, C. Dumard, T. Zemen, C. F. Mecklenbräuker, and A. F. Molisch, “A geometry-based stochastic MIMO model for vehicle-to-vehicle communications,” IEEE Transactions on Wireless Communications, vol. 8, no. 7, pp. 3646 – 3657, July 2009.

[29] A. Richter, “Estimation of radio channel parameters: Models and algorithms,” Ph.D. dissertation, Technischen Universität Ilmenau, 2005.

[30] B. H. Fleury, M. Tschudin, R. Heddergott, D. Dahlhaus, and K. I. Pedersen, “Channel parameter estimation in mobile radio environments using the SAGE algorithm,” IEEE Journal on Selected Areas in Communications, vol. 17, no. 3, pp. 434 – 450, March 1999.

[31] D. P. Gaillot, E. Tanghe, P. Stefanut, J. Wout, M. Lienard, P. Degauque, and L. Martens, “Gaillot - accuracy of specular path estimates with ESPRIT and RiMAX in the presence of measurement-based diffuse multipath components,” in 5th European Conference on Antennas and Propagation (EuCAP), Rome (Italy), April 2011, pp. 3619 – 3622.

[32] A. Richter, J. Salmi, and V. Koivunen, “Distributed scattering in radio channels and its contribution to MIMO channel capacity,” in 1st European Conference on Antennas and Propagation (EuCAP), Nice (France), November 2006, pp. 1 – 7.

[33] R. Wang, O. Renaudin, R. M. Bernas, and A. F. Molisch, “Efficiency improvement for path detection and tracking algorithm in a time-varying channel,” in IEEE 82nd Vehicular Technology Conference (VTC), Boston (MA, USA), September 2015, pp. 1 – 5.

[34] A. Richter, J. Salmi, and V. Koivunen, “ML estimation of covariance matrix for tensor valued signals in noise,” in IEEE International Conference on Acoustics, Speech and Signal Processing (ICASSP), Las Vegas (NV, USA), April 2008, pp. 2349 – 2352.

[35] M. Landmann, M. Käske, and R. S. Thomä, “Impact of incomplete and inacurrate data models on high resolution parameter estimation in multidimensional channel sounding,” IEEE Transactions on Antennas and Propagation, vol. 60, no. 2, pp. 557– 573, February 2012.

[36] A. F. Molisch, “A generic channel model for MIMO wireless propagation channels in macro- and microcells,” IEEE Transactions on Signal Processing, vol. 52, no. 1, pp. 61 – 71, January 2004.

[37] O. Renaudin, “Experimental channel characterization for vehicle-to-vehicle communication systems,” Ph.D. dissertation, Université catholique de Louvain, 2013.

[38] “802.11e-2005 - iEEE standard for information technology – Local and metropolitan area networks – Specific requirements Part 11: Wireless LAN Medium Access Control (MAC) and Physical layer (PHY) specifications - Amendment 8: Medium Access Control (MAC) quality of service enhancements,” IEEE Standards Association, November 2005, e-ISBN: 978-0-7381-4789-5.